

FORWARD AND TIME-REVERSED FULL-FIELD APPROXIMATION FOR FINITE-SIZE ACOUSTIC APERTURES

ASHKAN JAVAHERIAN AND SEYED KAMALEDDIN SETAREHDAN

Department of Biomedical Engineering, School of Electrical and Computer Engineering, College of Engineering, University of Tehran, Tehran, Iran.

ABSTRACT

The acoustic wave equation describes the wavefield in terms of volumetric radiation sources (s) or surface sources. For surface sources, boundary value problems yield wavefield descriptions using Kirchhoff-Helmholtz or Rayleigh-Sommerfeld integrals. A rigid-baffle assumption for the surface source results in an integral involving a monopole source, either as $-\partial p/\partial \mathbf{n}$ or $\rho_0 \partial(\mathbf{u} \cdot \mathbf{n})/\partial t$, while a soft-baffle assumption leads to an integral involving a dipole source, p . These source quantities are confined to a surface. Here, p represents the pressure, ρ_0 is the ambient density, \mathbf{u} is the velocity vector, and \mathbf{n} is the unit normal vector to the surface. This study establishes an equivalence between the analytic forms of monopole and dipole integral formulas and their full-field approximations. From an inverse problems perspective, this equivalence is crucial, as the full-field approximation of the time-reversed interior-field dipole integral formula acts as a time-reversal operator when receivers have finite sizes.

1. INTRODUCTION

The acoustic wave equation is one of the most important partial differential equations (PDEs) in mechanics [1, 2, 3, 4, 5, 6, 7, 8, 9], with a broad range of applications [10, 11, 12, 13, 14, 15, 16, 17, 18, 19, 20, 21, 22]. The forcing term on the right-hand side of this second-order PDE can be either time-instantaneous or time-varying. In biomedical applications, one notable example of a time-instantaneous acoustic source is the photoacoustic (PA) effect, a process involving the absorption of optical energy, its conversion to heat, and the generation of local acoustic pressures through thermoelastic expansion. Since the PA effect, which causes localized pressure increases, occurs on a timescale several orders of magnitude shorter than the propagation time of acoustic waves, the acoustic source can be approximated as time-instantaneous [23, 24, 25, 26, 27, 28, 29, 30, 31, 32, 33, 34, 35, 36, 37, 38]. For time-varying sources, a key example is the radiation from vibrating acoustic apertures. The modeling of time-varying sources has gained significant attention in biomedical applications, such as the back-projection step in photoacoustic tomography [23, 28, 29], the modeling of forward and adjoint operators in quantitative ultrasound tomography using full-field inversion approaches [39, 40, 41, 42, 43, 44, 45, 46, 47, 48, 49, 50], and treatment planning with focused ultrasound, an emerging technology for treating medical disorders by targeting deep tissues with ultrasonic energy [51, 52, 53, 54, 55, 56, 57, 58]. For the latter, accurate solutions to the wave equation are critical for ensuring safety [59, 60].

E-mail address: ashkan.javaherian@ut.ac.ir.

Date: January 2025.

The solution to the wave equation is typically non-unique. To obtain a unique solution, Cauchy initial conditions, defined in terms of the wavefield and its time derivative at the initial time, are enforced. These initial conditions establish a causal relationship between the solution wavefield and the source, ensuring that the solution wavefield vanishes prior to the onset of radiation from the source. Thus, solving the wave equation can be formulated as uniquely representing the propagated wavefield in terms of the radiation source (forcing term) by applying the causality conditions.

Let us delve into this problem in more detail. Let $d \in \{2, 3\}$ denote the number of dimensions of the medium. The radiation source, s , is defined over a finite d -dimensional space (a volume for $d = 3$) and time, and is assumed to possess finite energy, i.e., it is square-integrable over both space and time. Furthermore, the wavefield may be represented in terms of a surface source [61, 62], which bounds a volumetric radiation source or is mounted on an infinite plane. The wavefield induced by a source confined to a surface can be described using the *Kirchhoff-Helmholtz* or *Rayleigh-Sommerfeld* integral formulas, where the integration is carried out over the source’s surface, referred to here as the *acoustic aperture*. The former integral is suitable for apertures with arbitrary geometries, such as spheres or cylinders, while the latter is used for infinite-plane apertures.

Typically, the integrand in these formulas is a function of the pressure and its normal derivative over the surface. However, since the wave equation establishes a dependency between these quantities on the surface, the solution wavefield is well-defined if the associated integral formula is expressed in terms of only one of these quantities, i.e., either the pressure or its normal derivative. Consequently, to obtain a unique solution using these surface integral formulas, in addition to enforcing Cauchy conditions that satisfy causality, boundary conditions must also be imposed on the chosen solution space. The choice of the solution space and the boundary conditions depends on the physics of the problem.

For example, consider a vibrating piston surrounded by a *rigid baffle*, where the normal derivatives $\partial p / \partial \mathbf{n}$ vanish everywhere on the baffle except at the acoustic aperture, which is the front face of the vibrating piston. In this case, a *monopole* (or *singlet*) source can be defined in terms of the negative normal pressure derivative $-\partial p / \partial \mathbf{n}$, or equivalently $\rho_0 \partial(\mathbf{u} \cdot \mathbf{n}) / \partial t$ [39], over the surface. Here, ρ_0 represents the ambient density, \mathbf{u} is the velocity vector, and \mathbf{n} is the unit normal vector to the surface. This representation is known as the *monopole* integral formula.

On the other hand, under a *soft-baffle* assumption, the pressure p vanishes everywhere on the baffle except at the acoustic aperture. Consequently, the wavefield is defined in terms of a *dipole* (or *doublet*¹) surface source p . The *soft-baffle* representation depends on the normal derivatives of the Green’s function on the aperture’s surface and is referred to as the *dipole* integral formula.

Furthermore, it can be shown that a wavefield *back-projected* from an arbitrarily shaped bounding surface, such as a sphere or cylinder, can be described using an *Interior-field* variant of the *Kirchhoff-Helmholtz* integral formula. Similarly, a wavefield *back-projected* from an infinite-plane surface can be represented using an *Interior-field Rayleigh-Sommerfeld* integral formula.

It will be shown that a full-field approximation of the propagation of a time-varying ultrasonic pulse induced by a finite-size acoustic aperture can be expressed as a superposition of the actions of a causal (or diverging) Green’s function on a monopole (singlet) surface source, $\rho_0 \partial(\mathbf{u} \cdot \mathbf{n}) / \partial t$, or alternatively as the actions of the normal derivatives of the causal Green’s function on a dipole (doublet) surface source, p . For a d -dimensional acoustic medium, the source is confined to a $(d - 1)$ -dimensional surface. (For a radiation source s , the causal Green’s function acts on the d -dimensional space—volume for $d = 3$ —of the source’s support.)

¹The terms “singlet” (or “doublet”) source are less commonly used but encompass more general cases than the terms “monopole” (or “dipole”) source, respectively.

For a full-field approximation of the acoustic wave equation, it will be demonstrated how the actions of the causal Green’s function on the monopole source confined to a surface are defined in terms of a mass source term, which is added to the equation of continuity.

In addition, the dipole formula depends on the normal derivatives of the Green’s function on the surface of the aperture. In an analytic framework, these normal derivatives are functions of the *obliquity factor*, or equivalently the *solid angle*, which represents the angle subtended by an elemental area on the surface of the source as seen from arbitrary points in the solution space. It will be shown how the actions of the normal derivatives of the Green’s function on a dipole source (scalar pressure p , confined to a surface) can be defined in terms of a volumetric, vector-valued force source term, which is added to the equation of motion in the associated system of wave equations.

Most importantly, this work demonstrates that the resulting system of wave equations, incorporating an equation of motion with a volumetric, vector-valued force source, can be utilized to represent an *interior-field* formulation of the *dipole integral* formula. The time-reversed counterpart of this system functions as a *back-projection* or *time-reversal* operator, capturing the analytic angular dependence of finite-size receivers. Given that modeling acoustic apertures as point sources may lack sufficient accuracy at high frequencies [6, 7, 63, 64], particularly in biomedical applications [65, 66], the proposed *time-reversal* operator presents a compelling choice for incorporation into iterative frameworks, such as error minimization algorithms [26, 27, 29] or *Neumann series* iterations [23, 28], to solve associated inverse problems where receiver sizes are finite.

Outline. Section 2 introduces the wave equation in the time domain. This section explains how a unique solution to the wave equation can be obtained using homogeneous Cauchy conditions, which establish a causal relationship between the solution wavefield and a radiation source. A *primary* solution, describing the propagated wavefield in terms of a d -dimensional (volumetric for $d = 3$) radiation source, will be presented, and a *Kirchhoff-Helmholtz* solution, representing the wavefield in terms of a surface source, will be derived. It will be shown how *Dirichlet* or *Neumann* boundary conditions can be imposed to obtain unique solutions for an over-determined formula arising from the *Kirchhoff-Helmholtz* solution.

Section 3 describes the *primary* and *Kirchhoff-Helmholtz* solutions in the frequency domain. Additionally, a *Rayleigh-Sommerfeld* solution will be explained for cases where the surface source is mounted on an infinite, flat plane.

Section 4 describes how the time-domain variants of these surface integral formulas can be expressed as a summation of the actions of a causal Green’s function on a singlet surface source or the actions of the normal derivative of the Green’s function on a dipole surface source.

Section 5 explains how the derived time-domain analytical formulas can be incorporated into a full-field approach to approximate the solution wavefield in time and on a regular grid. This section details the definition and discretization of the mass and force sources and how these inputs are used in numerical systems to solve the wave equation in the time domain.

In Section 6, the time-domain variants of these analytic formulas will be compared to their full-field approximations on a regular grid.

Finally, Section 7 provides a brief summary of the numerical results. The section concludes with a discussion on the significance of the derived approach for incorporating sources into acoustic wave equations, particularly from the perspective of inverse problems.

2. WAVE EQUATION IN THE TIME DOMAIN

This section considers the propagation of acoustic waves from a real-valued space-and-time-varying source in an infinite, isotropic, and homogeneous medium in free space. Let $\mathbf{x} = [\mathbf{x}^1, \dots, \mathbf{x}^d]^T$ denote a spatial position in \mathbb{R}^d with $d \in \{2, 3\}$ as the number of dimensions. The analysis presented

here is performed for $d = 3$ but holds for $d = 2$ by replacing volumes with surfaces and surfaces with lines. (For instance, a line source in a 3D medium produces acoustic waves that propagate as cylindrical waves, equivalent to an omnidirectional point source in a 2D medium.)

The real-valued wavefield satisfies the inhomogeneous wave equation, expressed as

$$\frac{1}{c^2} \frac{\partial^2}{\partial t^2} p(\mathbf{x}, t) - \rho_0 \nabla \cdot \left[\frac{1}{\rho_0} \nabla p(\mathbf{x}, t) \right] = s(\mathbf{x}, t). \quad (1)$$

Here, the term on the right-hand side, $s(\mathbf{x}, t)$, is the forcing term, referred to as the *radiation source*, which is compactly supported in $\chi_s = \{\mathbf{x} \in \nu_s, t \in [0, T_s]\}$. Here, ν_s is a d -dimensional space (a volume for $d = 3$), and $[0, T_s]$ denotes the radiation time of the source. The radiation source s has units of $\text{kg m}^{-d} \text{s}^{-2}$ and is assumed to be square-integrable over χ_s .

Additionally, c represents the velocity of wave propagation in the medium (units: ms^{-1}), and ρ_0 denotes the ambient density of the medium (units: kg m^{-d}). The pressure wavefield p , the unknown parameter of the wave equation, has units of $\text{kg m}^{2-d} \text{s}^{-2}$ (or Pascal).

Assuming a constant value for ρ_0 , the wave equation (1) simplifies to its canonical form:

$$\left[\frac{1}{c^2} \frac{\partial^2}{\partial t^2} - \nabla^2 \right] p(\mathbf{x}, t) = s(\mathbf{x}, t). \quad (2)$$

2.1. Cauchy Conditions for Unique Solution. Typically, the solution to the wave equation is nonunique. A unique solution is obtained by confining the wavefield to a particular solution that is causally related to the source, i.e., a wavefield p that vanishes prior to the initial time $t = 0$ of the source radiation. By imposing the Cauchy conditions

$$p_+(\mathbf{x}, t)|_{t=0} = 0, \quad \frac{\partial}{\partial t} p_+(\mathbf{x}, t)|_{t=0} = 0, \quad (3)$$

a causal solution to the wave equation (2) is obtained, where the subscript $+$ denotes causality. Solving the inhomogeneous wave equation (2) with the causality conditions (Cauchy conditions (3)) is referred to as the *radiation problem*.

By contrast, if the forcing term s is set to zero, and the Cauchy conditions (3) are replaced with arbitrary and inhomogeneous fields at $t = 0$, the wave equation (2) becomes an *initial-value problem*, which arises, for instance, in photo-acoustic tomography.

2.2. Green's Function Solution to the Wave Equation. Consider the wave equation (2) as a radiation problem for a particular choice of source, $s(\mathbf{x}, t) = \delta(\mathbf{x} - \mathbf{x}')\delta(t - t')$, where $\delta(\cdot)$ is the Dirac delta function, and \mathbf{x}' and t' are free parameters in the space and time domains, respectively. In an infinite free space, the Green's function solution to the wave equation satisfies

$$\left[\frac{1}{c^2} \frac{\partial^2}{\partial t^2} - \nabla^2 \right] g(\mathbf{x} - \mathbf{x}', t - t') = \delta(\mathbf{x} - \mathbf{x}')\delta(t - t'). \quad (4)$$

For brevity, the Green's function will now be written in the form

$$g(\mathbf{x}_\diamond, t_\diamond) = g(\mathbf{x} - \mathbf{x}', t - t'), \quad (5)$$

where $\mathbf{x}_\diamond = \mathbf{x} - \mathbf{x}'$ and $t_\diamond = t - t'$. Similar to the wave equation (2), a unique solution to Eq. (4) is obtained by assuming a causality condition for the Green's function, i.e., $g_+(\mathbf{x}_\diamond, t_\diamond) = 0$ for $t_\diamond < 0$. For $d = 3$, the causal Green's function satisfies

$$g_+(\mathbf{x}_\partial, t_\partial) = \frac{1}{4\pi} \frac{\delta(t_\partial - \frac{x_\partial}{c})}{x_\partial}, \quad (6)$$

where $x_\partial = |\mathbf{x}_\partial|$.

Rewriting the wave equations (2) and (4) in the forms

$$\left[\frac{1}{c^2} \frac{\partial^2}{\partial t'^2} - \nabla_{\mathbf{x}'}^2 \right] p_+(\mathbf{x}', t') = s(\mathbf{x}', t'), \quad (7)$$

and

$$\left[\frac{1}{c^2} \frac{\partial^2}{\partial t'^2} - \nabla_{\mathbf{x}'}^2 \right] g(\mathbf{x} - \mathbf{x}', t - t') = \delta(\mathbf{x} - \mathbf{x}') \delta(t - t'), \quad (8)$$

where \mathbf{x} and t are fixed parameters in a closed set $\chi = \{\mathbf{x} \in \nu, t \in [t_0, t_1]\}$, within which the solution is sought.

Now, multiplying Eq. (7) by $g(\mathbf{x}_\partial, t_\partial)$ and Eq. (8) by $p_+(\mathbf{x}', t')$, then subtracting the modified Eq. (8) from the modified Eq. (7), yields [67]:

$$\frac{1}{c^2} \left[g \frac{\partial^2 p_+}{\partial t'^2} - \frac{\partial^2 g}{\partial t'^2} p_+ \right] - \left[g \nabla^2 p_+ - \nabla^2 g p_+ \right] = g s - \delta(\mathbf{x}_\partial) \delta(t_\partial) p_+. \quad (9)$$

Integrating the left-hand side of Eq. (9) over the spatio-temporal solution set χ gives

$$\frac{1}{c^2} \int_{t_0}^{t_1} dt' \int_{\nu} d\mathbf{x}' \frac{\partial}{\partial t'} \left[g \frac{\partial p_+}{\partial t'} - \frac{\partial g}{\partial t'} p_+ \right] - \nabla \cdot \left[g \nabla p_+ - \nabla g p_+ \right]. \quad (10)$$

Taking the temporal integral of the first term in (10), applying Green's theorem to the second term, and integrating the right-hand side of Eq. (9) over χ gives [67]:

$$\begin{aligned} & \frac{1}{c^2} \int_{\nu} d\mathbf{x}' \left[g \frac{\partial p_+}{\partial t'} - \frac{\partial g}{\partial t'} p_+ \right] \Big|_{t'=t_0}^{t_1} - \int_{t_0}^{t_1} dt' \int_{\partial\nu} dS' \left[g \frac{\partial p_+}{\partial \mathbf{n}'} - \frac{\partial g}{\partial \mathbf{n}'} p_+ \right] = \\ & \int_{t_0}^{t_1} dt' \int_{\nu} d\mathbf{x}' g s - \begin{cases} p_+, & \text{if } \mathbf{x} \in \nu, t \in [t_0, t_1], \\ 0, & \text{otherwise,} \end{cases} \end{aligned} \quad (11)$$

where \mathbf{n}' is an outward unit normal vector to the surface $\partial\nu$.

2.2.1. Primary Solution. A primary solution for all space and all time can be obtained by choosing g as the causal Green's function, g_+ , and extending the spatio-temporal set χ to infinity. Accordingly, the limits $\nu \rightarrow \infty$, $t_0 \rightarrow -\infty$, and $t_1 \rightarrow \infty$ are taken.

For the first term on the left-hand side of Eq. (11), the assumption of causality ensures that p_+ vanishes at $t = -\infty$, and g vanishes at $t = +\infty$. As a result, this term drops out. Furthermore, since a causal Green's function satisfies $g(\mathbf{x}_\partial, t_\partial) = 0$ unless $x_\partial = ct_\partial$, the contribution from the surface $\partial\nu$ with an infinite radius vanishes for any finite and arbitrarily large value of t_1 [67]. Consequently, the second term on the left-hand side of Eq. (11) also vanishes.

Therefore, the primary solution for p_+ at any pair of \mathbf{x} and t lying in the set χ satisfies

$$p_+(\mathbf{x}, t) = \int_0^{T_s} dt' \int_{\nu_s} d\mathbf{x}' g_+(\mathbf{x}_\partial, t_\partial) s(\mathbf{x}', t'). \quad (12)$$

The *primary* formula (12) expresses the solution wavefield in terms of the radiation source s , which is the forcing term on the right-hand side of the wave equation. Given the assumption of infinite extension for the set χ , this solution holds over all space and all time.

2.2.2. Exterior-Field Kirchhoff-Helmholtz Solution. This section describes the *Kirchhoff-Helmholtz solution* to the wave equation. The underlying theory originated in optics to model light diffraction through small apertures on a dark screen and was later extended to acoustics to describe the radiation from a vibrating piston in a baffle. While the primary solution in Eq. (12) directly maps the forcing term s to the wavefield solution p_+ via an integral over the volumetric source support ν_s , many practical problems quantify the source over an external surface. For such cases, a more applicable formulation can be derived.

Consider a finite volume ν that contains the source volume ν_s and is bounded by a closed surface $\partial\nu$. The solution space is confined to the volume ν^c , which lies outside $\partial\nu$. Using the causality assumption for the solution p_+ in Eq. (7) over the time interval $[t_0, t_1]$, with $t_0 \rightarrow -\infty$ and $t_1 \rightarrow +\infty$, and applying the causality of the Green's function g_+ in Eq. (8), the solution procedure mirrors that in Section 2.2.1. However, the integral in Eq. (11) is now taken over ν^c instead of ν .

As before, the first term on the left-hand side of Eq. (11) vanishes due to the causality of p_+ and g_+ , and the contribution from the surface at infinite radius also vanishes, as discussed in Section 2.2.1. Consequently, the field p_+ in the solution space ν^c satisfies the following integral equation [67]:

$$\int_{-\infty}^{\infty} dt' \int_{\partial\nu} dS' \left[\left(\frac{\partial g_+}{\partial \mathbf{n}'} \right) p_+ - g_+ \left(\frac{\partial p_+}{\partial \mathbf{n}'} \right) \right] = \begin{cases} p_+(\mathbf{x}, t), & \mathbf{x} \in \nu^c, \\ 0, & \mathbf{x} \in \nu, \end{cases} \quad (13)$$

where \mathbf{n}' is the unit vector normal to the surface $\partial\nu$, directed outward from the interior volume ν to the exterior volume ν^c .

In Eq. (13), the formula for the exterior volume is known as the *first Helmholtz identity*. It describes the wavefield p_+ outside the surface $\partial\nu$ as a function of the field and its normal derivative over $\partial\nu$. The formula for the interior volume is referred to as the *second Helmholtz identity*, which is a homogeneous integral equation that relates the field to its normal derivative over the surface $\partial\nu$.

Due to the dependence established by the *second Helmholtz identity*, the *first Helmholtz identity* becomes an over-determined problem unless boundary conditions are imposed. To make the problem well-posed, the integrand in Eq. (13) must depend solely on the wavefield, its normal derivative, or a linear combination of both. These requirements are satisfied by imposing *Dirichlet*, *Neumann*, or *Mixed* boundary conditions, respectively.

2.2.3. Interior-Field Kirchhoff-Helmholtz Solution. The *Exterior-Field Kirchhoff-Helmholtz solution* describes the wavefield at points outside a closed surface $\partial\nu$ using the causal pressure field and its outward normal derivative on $\partial\nu$. This corresponds to a *forward propagation* problem. In this section, we address the *back-projection* or *time-reversal* problem, where the field is reconstructed within the interior region ν that contains the source.

For times greater than the source turn-off time T_s , the field within ν satisfies homogeneous (vanishing) Cauchy conditions and can be represented as a boundary-value problem. By confining

the space ν within a finite volume enclosed by $\partial\nu$ and taking the limits $t_0 \rightarrow -\infty$ and $t_1 \rightarrow +\infty$, the integral formula in Eq. (11) becomes:

$$\int_{-\infty}^{\infty} dt' \int_{\partial\nu} dS' \left[g_- \left(\frac{\partial p_+}{\partial \mathbf{n}'} \right) - \left(\frac{\partial g_-}{\partial \mathbf{n}'} \right) p_+ \right] = \begin{cases} p_+(\mathbf{x}, t), & \mathbf{x} \in \nu, \\ 0, & \mathbf{x} \in \nu^c, \end{cases} \quad t > T_s, \quad (14)$$

where \mathbf{n}' is the outward unit normal vector from ν into ν^c , and g_- is an *anti-causal* (or *incoming-wave*) Green's function.

Using the transformations $t \rightarrow -t$ and $t' \rightarrow -t'$, and redefining \mathbf{n}' as \mathbf{n}'_- , the inward normal vector from ν^c into ν , Eq. (14) transforms into:

$$\phi(\mathbf{x}, -t) = \int_{-\infty}^{\infty} dt' \int_{\partial\nu} dS' \left[\left(\frac{\partial g_+}{\partial \mathbf{n}'_-} \right) p_+(\mathbf{x}', -t') - g_+ \left(\frac{\partial p_+}{\partial \mathbf{n}'_-} \right) \right], \quad (15)$$

where $\phi(\mathbf{x}, -t)$ is the *back-projected* field. This field satisfies $\phi(\mathbf{x}, -t) = p_+(\mathbf{x}, -t)$ for $t < -T_s$, indicating that the time-reversed back-projected field is reconstructed within ν from the time-reversed wavefield measured on $\partial\nu$ for $t < -T_s$.

To ensure uniqueness, the surface integral in the interior region must use Green's functions that satisfy homogeneous *Neumann* or *Dirichlet* boundary conditions. In practical applications, since the measured quantity on the surface is typically the wavefield p , a homogeneous *Dirichlet* boundary condition is imposed on the Green's function in the back-projection (or time-reversal propagation) formula [65, 66].

3. WAVE EQUATION IN THE FREQUENCY DOMAIN

This section addresses the wave equation in the temporal frequency domain. The temporal Fourier transform and its inverse are defined as:

$$F(\mathbf{x}, \omega) = \int_{-\infty}^{\infty} dt f(\mathbf{x}, t) e^{i\omega t}, \quad f(\mathbf{x}, t) = \frac{1}{2\pi} \int_{-\infty}^{\infty} d\omega F(\mathbf{x}, \omega) e^{-i\omega t}. \quad (16)$$

Applying the temporal Fourier transform to Eq. (4) results in the *Helmholtz equation*:

$$\left[\frac{\omega^2}{c^2} + \nabla^2 \right] G(\mathbf{x}_\partial, \omega) = -\delta(\mathbf{x}_\partial), \quad (17)$$

where $G(\mathbf{x}_\partial, \omega)$ is the frequency-domain Green's function. The relationship between the time-domain and frequency-domain Green's functions is given by:

$$G(\mathbf{x}_\partial, \omega) = \int_{-\infty}^{\infty} dt_\partial g(\mathbf{x}_\partial, t_\partial) e^{i\omega t_\partial}, \quad g(\mathbf{x}_\partial, t_\partial) = \frac{1}{2\pi} \int_{-\infty}^{\infty} d\omega G(\mathbf{x}_\partial, \omega) e^{-i\omega t_\partial}. \quad (18)$$

3.1. Causality Condition and Outgoing Green's Function. Similar to Eq. (4), the inhomogeneous wave equation in Eq. (17) admits non-unique solutions, requiring additional constraints for uniqueness. The causality condition for the time-domain wave equation imposes a boundary condition at infinity in the frequency domain. The frequency-domain Green's function is derived through a spatio-temporal Fourier transform, yielding:

$$G_+(\mathbf{x}_\partial, \omega) = \frac{1}{4\pi} \frac{e^{ikx_\partial}}{x_\partial}, \quad (19)$$

where $x_{\mathfrak{d}} = |\mathbf{x}_{\mathfrak{d}}|$ and $k = \omega/c$ is the wavenumber. The subscript $+$ signifies that this is an *outgoing* Green's function. Substituting Eq. (19) into the inverse Fourier transform in Eq. (18) gives:

$$g_+(\mathbf{x}_{\mathfrak{d}}, t_{\mathfrak{d}}) = \frac{1}{2\pi} \int_{-\infty}^{\infty} d\omega \frac{1}{4\pi} \frac{e^{i\omega(\frac{x_{\mathfrak{d}}}{c} - t_{\mathfrak{d}})}}{x_{\mathfrak{d}}}. \quad (20)$$

In this expression, the time-domain Green's function is a superposition of time-harmonic waves with spherical surfaces of constant phase $x_{\mathfrak{d}} - ct_{\mathfrak{d}}$. These surfaces are *outgoing*, as increasing $t_{\mathfrak{d}}$ requires $x_{\mathfrak{d}}$ to increase proportionally, ensuring causality. Thus, the causal Green's function is inherently *outgoing* or *diverging* [67].

Remark 1. For 2D media, where \mathbf{x} represents a position in a plane, the equivalent causal Green's function satisfies:

$$G_+^{2D}(\mathbf{x}_{\mathfrak{d}}, \omega) = \frac{i}{4} H_0^+(kx_{\mathfrak{d}}) \approx \left[\frac{1}{8\pi kx_{\mathfrak{d}}} \right]^{1/2} e^{i(kx_{\mathfrak{d}} + \frac{\pi}{4})}, \quad kx_{\mathfrak{d}} \rightarrow \infty, \quad (21)$$

where $kx_{\mathfrak{d}}$ is the accumulated phase. This asymptotic expansion reflects the behavior of 2D Green's functions in homogeneous media.

3.2. Green's Function Solution to the Wave Equation. This section discusses solutions to the wave equation in the frequency domain. Similar to Section 2.2, the wavefield solution is first derived for a volumetric radiation source s . This solution is then extended to a wavefield defined in terms of a source over a surface enclosing a volumetric space ν_s , which represents the support of the radiation source.

3.2.1. Primary Solution. A primary solution to the inhomogeneous wave equation in the frequency domain is derived as follows. Substituting the inverse Fourier transform relation in Eq. (18) into the time-domain primary solution in Eq. (12) and applying the substitution:

$$S(\mathbf{x}', \omega) = \int_0^{T_s} dt' e^{i\omega t'} s(\mathbf{x}', t'), \quad (22)$$

results in the frequency-domain primary solution:

$$P_+(\mathbf{x}, \omega) = \int_{\nu_s} d\mathbf{x}' G_+(\mathbf{x}_{\mathfrak{d}}, \omega) S(\mathbf{x}', \omega), \quad (23)$$

where $t_{\mathfrak{d}} = t - t'$ has been used.

3.2.2. Exterior-Field Kirchhoff-Helmholtz Solution. The *Exterior-field Kirchhoff-Helmholtz* formula in the frequency domain is presented here. The corresponding *Interior-field* variant is left for the reader (see Section 2.2.3). The frequency-domain *Exterior-field Kirchhoff-Helmholtz* formula is given by [67]:

$$\int_{\partial\nu} dS' \left[\left(\frac{\partial}{\partial \mathbf{n}'} G_+(\mathbf{x}_{\mathfrak{d}}, \omega) \right) P_+(\mathbf{x}', \omega) - G_+(\mathbf{x}_{\mathfrak{d}}, \omega) \left(\frac{\partial}{\partial \mathbf{n}'} P_+(\mathbf{x}', \omega) \right) \right] = \begin{cases} P_+(\mathbf{x}, \omega), & \mathbf{x} \in \nu^{\mathcal{C}}, \\ 0, & \mathbf{x} \in \nu, \end{cases} \quad (24)$$

where \mathbf{n}' is the outward unit normal vector from the interior volume ν , containing the source volume ν_s , to the exterior volume $\nu^{\mathcal{C}}$, which is the solution space.

As discussed in Section 2.2.2, for $\mathbf{x} \in \nu^{\mathcal{C}}$, Eq. (24) is termed the *first Helmholtz identity*. This identity is over-determined because the surface integral for $\mathbf{x} \in \nu$, known as the *second Helmholtz identity*, vanishes. Consequently, a dependence arises between the field and its normal derivative over $\partial\nu$. To make the solution in $\nu^{\mathcal{C}}$ well-posed, boundary conditions must be imposed on the surface $\partial\nu$.

By imposing *Neumann* and *Dirichlet* boundary conditions, the formula in Eq. (24) simplifies into two distinct forms.

The *monopole formula*, based on the Neumann boundary condition, is expressed as:

$$P_+^N(\mathbf{x}, \omega) = - \int_{\partial\nu} dS' G_+^N(\mathbf{x}_\partial, \omega) \left(\frac{\partial}{\partial \mathbf{n}'} P_+(\mathbf{x}', \omega) \right), \quad (25)$$

where $\frac{\partial}{\partial \mathbf{n}'} G_+^N(\mathbf{x}_\partial, \omega)|_{\mathbf{x}' \in \partial\nu} = 0$. This formula models the rigid-baffle condition, where the normal derivative of the wavefield vanishes on the baffle surface, except on the front face of the vibrating piston, known as the *acoustic aperture*. The acoustic aperture is the only region where energy is radiated.

The *dipole formula*, derived under the Dirichlet boundary condition, is given by:

$$P_+^D(\mathbf{x}, \omega) = \int_{\partial\nu} dS' \left(\frac{\partial}{\partial \mathbf{n}'} G_+^D(\mathbf{x}_\partial, \omega) \right) P_+(\mathbf{x}', \omega), \quad (26)$$

with $G_+^D(\mathbf{x}_\partial, \omega)|_{\mathbf{x}' \in \partial\nu} = 0$. This corresponds to a scenario where the wavefield itself vanishes on the baffle surface, except at the acoustic aperture, as in the case of a piston vibrating in a soft baffle.

Here, $\mathbf{x} \in \nu^c$, and G_+^N and G_+^D denote causal Green's functions satisfying the homogeneous Neumann and Dirichlet boundary conditions, respectively, on $\partial\nu$. These boundary conditions ensure that the behavior of the wavefield over the acoustic aperture uniquely determines the solution in the exterior domain.

3.2.3. Exterior-field Rayleigh-Sommerfeld solution. The *Rayleigh-Sommerfeld* integral formula arises from solving the boundary-value problem of the Helmholtz wave equation under the assumption of a source mounted on an infinite planar surface. To derive this formula, the solution space is defined as a half-space bounded by an infinite plane, denoted as $\partial\nu$, and an infinite-radius hemisphere. For simplicity, the bounding plane is taken as $\mathbf{x}^3 = 0$, and the solution is sought in the half-space $\mathbf{x}^3 > 0$.

As discussed previously, the associated *Kirchhoff-Helmholtz* integral formula is over-determined. To make this problem well-posed, boundary conditions of the *Dirichlet* or *Neumann* form must be imposed on the plane $\partial\nu$. A common method for addressing this boundary-value problem is the *method of images* [67]. Here, \mathbf{x} and \mathbf{x}' represent the positions of the general field point and the source point in the 3D medium, respectively, with both assumed to lie in the half-space $\nu^+ = \{\mathbf{x} : \mathbf{x}^3 > 0\}$.

For the source point $\mathbf{x}' = [\mathbf{x}'^1, \mathbf{x}'^2, \mathbf{x}'^3]^T$, a mirror-image source point $\tilde{\mathbf{x}}' = [\mathbf{x}'^1, \mathbf{x}'^2, -\mathbf{x}'^3]^T$ is introduced, ensuring that \mathbf{x} and $\tilde{\mathbf{x}}'$ lie on opposite sides of the plane. Consequently, $\delta(\mathbf{x} - \tilde{\mathbf{x}}') = 0$. The Helmholtz equation with an augmented forcing term is then defined as:

$$[k^2 + \nabla_{\mathbf{x}}^2] G_+^N(\mathbf{x} - \mathbf{x}', \omega) = -\delta(\mathbf{x} - \mathbf{x}') - \delta(\mathbf{x} - \tilde{\mathbf{x}}'), \quad (27)$$

where the Green's function G_+^N satisfies:

$$G_+^N(\mathbf{x} - \mathbf{x}', \omega) = G_+(\mathbf{x} - \mathbf{x}', \omega) + G_+(\mathbf{x} - \tilde{\mathbf{x}}', \omega). \quad (28)$$

This augmented Green's function vanishes on the infinite-radius hemisphere. For a source point \mathbf{x}' approaching the plane $\mathbf{x}^3 = 0$, it follows that $|\mathbf{x} - \tilde{\mathbf{x}}'| = |\mathbf{x} - \mathbf{x}'|$. Consequently, the Green's function satisfies:

$$G_+^N(\mathbf{x}_\partial, \omega)|_{\mathbf{x}' \in \partial\nu} = 2G_+(\mathbf{x}_\partial, \omega)|_{\mathbf{x}' \in \partial\nu}, \quad \frac{\partial}{\partial \mathbf{n}'} G_+^N(\mathbf{x}_\partial, \omega)|_{\mathbf{x}' \in \partial\nu} = 0. \quad (29)$$

Substituting G_+^N into the *Kirchhoff-Helmholtz* formula yields the monopole formula:

$$P_+^N(\mathbf{x}, \omega) = -a_p \int_{\partial\nu} dS' G_+^N(\mathbf{x}_\nu, \omega) \left(\frac{\partial}{\partial \mathbf{n}'} P_+(\mathbf{x}', \omega) \right), \quad (30)$$

where $a_p = 2$. Here, $\mathbf{x} \in \nu^+$, the solution half-space $\{\mathbf{x} : \mathbf{x}^3 > 0\}$, and \mathbf{n}' is the unit normal vector to the plane $\mathbf{x}^3 = 0$, directed into the solution space ν^+ . The integral is evaluated over the surface $\partial\nu = \{\mathbf{x} : \mathbf{x}^3 = 0\}$.

Alternatively, imposing a homogeneous *Dirichlet* boundary condition for the Green's function on $\partial\nu$ results in the dipole formula:

$$P_+^D(\mathbf{x}, \omega) = a_p \int_{\partial\nu} dS' \left(\frac{\partial}{\partial \mathbf{n}'} G_+^D(\mathbf{x}_\nu, \omega) \right) P_+(\mathbf{x}', \omega), \quad (31)$$

where $G_+^D(\mathbf{x}_\nu, \omega)|_{\mathbf{x}' \in \partial\nu} = 0$ and $a_p = 2$.

The monopole formula in Eq. (30) corresponds to the *rigid-baffle* condition, where the normal derivative of the wavefield vanishes on the baffle except on the acoustic aperture. Similarly, the dipole formula in Eq. (31) corresponds to the *soft-baffle* condition, where the wavefield itself vanishes everywhere except on the acoustic aperture.

4. TIME-DOMAIN MONOPOLE AND DIPOLE FORMULAS IN TERMS OF A SUMMATION OF ACTIONS OF THE CAUSAL GREEN'S FUNCTION ON A SURFACE SOURCE

This section is added to explicitly derive the well-determined Green's function solutions to the wave equation in terms of the actions of the causal Green's function.

4.1. Monopole formula. As discussed earlier, the monopole formula is based on the assumption of a vibrating piston mounted on a rigid baffle. This assumption implies that the normal derivative of the wavefield vanishes on the baffle except within the aperture. Correspondingly, using a causal Green's function g_+^N , which satisfies a homogeneous *Neumann* boundary condition over the surface $\partial\nu$ bounding the source, the integral over that surface depends only on the normal pressure derivative $-\partial p_+ / \partial \mathbf{n}'$, representing a monopole source. Accordingly, the monopole variants of *Kirchhoff-Helmholtz* or *Rayleigh-Sommerfeld* formulas yield in the time domain:

$$p_+^N(\mathbf{x}, t) = a_p \int_0^{T_s} dt' \int_{\partial\nu} dS' g_+^N(\mathbf{x}_\nu, t_\nu) \left[\rho_0 \frac{\partial}{\partial t} u^n(\mathbf{x}', t') \right], \quad (32)$$

where the replacement

$$\frac{\partial}{\partial \mathbf{n}'} p = -\rho_0 \frac{\partial}{\partial t} u^n, \quad (33)$$

with $u^n = \mathbf{u} \cdot \mathbf{n}$, has been used. Here, ρ_0 is the mass density, and u^n is the normal component of the velocity vector \mathbf{u} over the surface. Additionally, for the *Exterior-field Kirchhoff-Helmholtz* solution, $\mathbf{x} \in \nu^C$ and $a_p = 1$, and for the *Exterior-field Rayleigh-Sommerfeld* solution, $\mathbf{x} \in \nu^+$ and $a_p = 2$ are used. The former and latter apply to arbitrary-shaped (non-plane) and flat-plane apertures, respectively.

4.2. Dipole formula. The dipole formula is derived under the assumption of a soft baffle, on which the pressure vanishes everywhere except the front face of the vibrating piston. Correspondingly, using a causal Green's function g_+^D , which satisfies a homogeneous *Dirichlet* boundary condition over $\partial\nu$, the integral formula depends only on the wavefield p_+ , representing a dipole source, when confined to a surface. For analytic (or ray-based) methods used to approximate the dipole integral formula, it is convenient to reformulate the formula in terms of weighted actions of the causal

Green's function. Substituting the time-domain Green's function (6) into the dipole variants of the *Kirchhoff-Helmholtz* or *Rayleigh-Sommerfeld* formulas yields:

$$p_+^D(\mathbf{x}, t) = a_p \int_0^{T_s} dt' \int_{\partial\nu} dS' [\mathbf{n}' \cdot \nabla_{\mathbf{x}'} g_+^D(\mathbf{x}_\partial, t_\partial)] p(\mathbf{x}', t'), \quad (34)$$

$$= a_p \int_0^{T_s} dt' \int_{\partial\nu} dS' [\mathbf{n}' \cdot \frac{\mathbf{x}_\partial}{x_\partial}] g_+(\mathbf{x}_\partial, t_\partial) \frac{1}{c} \left[\frac{\partial}{\partial t'} + \frac{1}{t_\partial} \right] p(\mathbf{x}', t'), \quad (35)$$

where $\mathbf{x}_\partial = \mathbf{x} - \mathbf{x}'$ is the distance vector. Here, $\mathbf{n}' \cdot \mathbf{x}_\partial / x_\partial$ is the *obliquity factor*, which weights the actions of the Green's function on a surface source split into *far-field* and *near-field* terms. In Eq. (34), applying a *far-field approximation* $kx_\partial \gg 1$, equivalent to $\partial p / \partial t' \gg p / t_\partial$ in the time domain, valid in regions sufficiently far from the aperture, allows neglecting the p / t_∂ term. Thus, a *far-field approximation* of Eq. (35) becomes:

$$p_+^D(\mathbf{x}, t) \approx a_p \int_0^{T_s} dt' \int_{\partial\nu} dS' [\mathbf{n}' \cdot \frac{\mathbf{x}_\partial}{x_\partial}] g_+(\mathbf{x}_\partial, t_\partial) \left[\frac{1}{c} \frac{\partial}{\partial t'} p(\mathbf{x}', t') \right]. \quad (36)$$

It should be noted that $a_p = 1$ and $a_p = 2$ are used for the *Kirchhoff-Helmholtz* and *Rayleigh-Sommerfeld* formulas, respectively.

Remark 2. Using ray-based methods, it is computationally more efficient to express the integral formula (35) in terms of a solid angle element $d\Omega_{\mathbf{x}}(S'(\mathbf{x}'))$, defined as the angle subtended by an infinitesimal area dS' corresponding to the point \mathbf{x}' on the surface of the aperture, as seen from any arbitrary field point \mathbf{x} . The solid angle relates to the obliquity factor through the formula:

$$d\Omega_{\mathbf{x}}(S'(\mathbf{x}')) = \frac{dS'}{x_\partial^2} [\mathbf{n}' \cdot \frac{\mathbf{x}_\partial}{x_\partial}]. \quad (37)$$

Using full-field approaches, it will be shown how a vector-valued force source can be defined and incorporated into an equation of motion so that the resulting system of wave equations directly approximates the original dipole integral formula (34).

5. FULL-FIELD APPROXIMATION OF THE WAVE EQUATION IN THE TIME DOMAIN

This section presents a full-field approximation of the acoustic wave equation (1). Specifically, it introduces a semi-numerical framework for approximating the time-domain *Primary solution* (12) of the wave equation, which directly relates a causal wavefield to a d -dimensional radiation source s . Furthermore, the semi-numerical system is extended to describe the wavefield in terms of sources confined to a $(d - 1)$ -dimensional surface, allowing solutions of the *monopole* integral formula (32) and the *dipole* integral formula (34).

5.1. Systems of Coupled Wave Equations. This subsection outlines a semi-numerical system for approximating the time-domain *Primary solution* derived in Eq. (12). To achieve this, we begin by transferring the spatial gradient terms to the right-hand side of the wave equation (1), yielding

$$\frac{1}{c^2} \frac{\partial^2}{\partial t^2} p(\mathbf{x}, t) = \rho_0 \nabla \cdot \left[\frac{1}{\rho_0} \nabla p(\mathbf{x}, t) \right] + s(\mathbf{x}, t), \quad (38)$$

where s is a finite-volume source that radiates within a finite time and is square-integrable over the space-time domain.

5.1.1. *System of Wave Equations for solving the Primary formula.* The wave equation (38) can be reformulated into coupled first-order equations, resulting in the time-stepping system [2]:

$$\begin{aligned}\frac{\partial}{\partial t}\mathbf{u}(\mathbf{x}, t) &= -\frac{1}{\rho_0}\nabla p(\mathbf{x}, t), \\ \frac{\partial}{\partial t}\rho(\mathbf{x}, t) &= -\rho_0\nabla \cdot \mathbf{u}(\mathbf{x}, t) + s_m(\mathbf{x}, t), \\ p(\mathbf{x}, t) &= c^2\rho(\mathbf{x}, t).\end{aligned}\tag{39}$$

where the first two lines are approximated using numerical integration in time. The input to this system is the *mass source* s_m , which is related to the radiation source s by:

$$s(\mathbf{x}, t) = \frac{\partial}{\partial t}s_m(\mathbf{x}, t) \Leftrightarrow s_m(\mathbf{x}, t) = \int_0^t dt' s(\mathbf{x}, t').\tag{40}$$

Here, s_m has units of $\text{kg m}^{-d}\text{s}^{-1}$.

5.1.2. *System of Coupled Wave Equations for solving the surface integral formulas.* The coupled first-order wave equations (38) can be used to describe the wavefield in terms of surface sources through the monopole and dipole integral formulas:

$$\begin{aligned}\frac{\partial}{\partial t}\mathbf{u}(\mathbf{x}, t) &= -\frac{1}{\rho_0}\nabla p(\mathbf{x}, t) + \mathcal{S}_f(\mathbf{x}, t), \\ \frac{\partial}{\partial t}\rho(\mathbf{x}, t) &= -\rho_0\nabla \cdot \mathbf{u}(\mathbf{x}, t) + \mathcal{S}_m(\mathbf{x}, t), \\ p(\mathbf{x}, t) &= c^2\rho(\mathbf{x}, t).\end{aligned}\tag{41}$$

In this formulation, the first line is the equation of *motion* with \mathcal{S}_f representing a vector-valued force source, while the second line is the equation of *continuity* with \mathcal{S}_m remaining the scalar-valued mass source.

The following section describes how including a mass source \mathcal{S}_m in the equation of continuity within the wave equation system (41) allows for modeling the monopole integral formula. Furthermore, it explains how incorporating a vector-valued force source \mathcal{S}_f in the equation of motion enables the wave equation system to model the dipole integral formula (34).

5.2. Source Approximation. To define a source, we start with dividing the space of support of the source, which can be either a d -dimensional space ν_s , or a $(d-1)$ -dimensional space $\partial\nu$ (for $d=3$, a bounding surface or a flat plane), into a union of non-overlapping primitive shapes (elements) e , $e \in \{1, \dots, N_e\}$ with vertices j , $j \in \{1, \dots, N_j\}$. Accordingly, $l(e)$ denotes the set of vertices connected to element e , and has $N_{l(e)}$ members. For $d=3$ and a volumetric (resp. surface) source, the elements are set to tetrahedrons (resp. triangles). (The volumetric (resp. surface) source for $d=3$ is reduced to a surface (resp. line) source for $d=2$.) In addition, here we introduce $\delta_b(\mathbf{x}) \in C^\infty$ as an infinitely differentiable approximation of the Dirac delta function $\delta(\mathbf{x})$. The choice for δ_b is affected by discretization and will be discussed later.

5.2.1. *s_m in terms of a d -dimensional radiation source s .* For numerically approximating the time-domain primary formula (12), a mass source in terms of the radiation source s can be approximated

using the formula

$$\begin{aligned} s_m(\mathbf{x}, t) &= \int_{\nu_s} d\mathbf{x}' \delta(\mathbf{x} - \mathbf{x}') \left[\int_0^t dt' s(\mathbf{x}', t') \right] \\ &\approx \frac{1}{N_{l(e)}} \sum_{e=1}^{N_e} v_e \sum_{j \in l(e)} \delta_b(\mathbf{x} - \mathbf{x}_j) \left[\int_0^t dt' s(\mathbf{x}_j, t') \right], \quad \mathbf{x}_j \in \nu_s. \end{aligned} \quad (42)$$

In Eq. (42), for $d = 3$, the element e is a tetrahedron with v_e the volume of element e , and $N_{l(e)} = d + 1$, i.e., e has $d + 1$ connected vertices.

For each individual node j , solving the system (41) with a mass source defined by Eq. (42) is equivalent to solving the wave equation:

$$\left[\frac{1}{c^2} \frac{\partial^2}{\partial t^2} - \nabla^2 \right] \tilde{p}(\mathbf{x}, t) \approx \delta_b(\mathbf{x} - \mathbf{x}_j) s(\mathbf{x}_j, t), \quad (43)$$

where \tilde{p} has the nonphysical units of Pa m⁻² due to the omission of the surface integral.

5.2.2. \mathcal{S}_m in terms of a $(d - 1)$ -dimensional monopole source $\rho_0 \mathbf{u}^n$. For numerically approximating the monopole integral formula (32), a generalized mass source is defined in the form

$$\begin{aligned} \mathcal{S}_{(m, \mathbf{u}^n)}(\mathbf{x}, t) &= a_p \int_{\partial\nu} dS'(\mathbf{x}') \delta(\mathbf{x} - \mathbf{x}') [\rho_0 \mathbf{u}(\mathbf{x}, t) \cdot \mathbf{n}'(\mathbf{x})] \\ &\approx \frac{a_p}{N_{l(e)}} \sum_{e=1}^{N_e} s_e \sum_{j \in l(e)} \delta_b(\mathbf{x} - \mathbf{x}_j) [\rho_0 \mathbf{u}(\mathbf{x}_j, t) \cdot \mathbf{n}(\mathbf{x}_j)], \quad \mathbf{x}_j \in \partial\nu. \end{aligned} \quad (44)$$

For each individual node j , solving the system (41) with a mass source defined by Eq. (44) is equivalent to solving the wave equation:

$$\left[\frac{1}{c^2} \frac{\partial^2}{\partial t^2} - \nabla^2 \right] \tilde{p}(\mathbf{x}, t) \approx \delta_b(\mathbf{x} - \mathbf{x}_j) \left[\rho_0 \frac{\partial \mathbf{u}(\mathbf{x}_j, t)}{\partial t} \cdot \mathbf{n}(\mathbf{x}_j) \right], \quad (45)$$

where \tilde{p} has nonphysical units of Pa m⁻² due to the omission of the surface integral.

5.2.3. \mathcal{S}_m in terms of a $(d - 1)$ -dimensional dipole source p . As discussed above, by a far-field approximation $kx_\delta \gg 1$, the dipole formula (34) is reduced to the formula (36). In some literature, by an assumption $\mathbf{n}' \cdot [\mathbf{x}_\delta / x_\delta] = 1$, which is equivalent to assuming the acoustic aperture omnidirectional, a full-field approximation of the formula (36) has been done using the semi-numerical system (41), and a generalized mass source

$$\begin{aligned} \mathcal{S}_{(m, p)}(\mathbf{x}, t) &= a_p \int_{\partial\nu} dS'(\mathbf{x}') \delta(\mathbf{x} - \mathbf{x}') \left[\frac{1}{c} p(\mathbf{x}', t) \right] \\ &\approx \frac{a_p}{N_{l(e)}} \sum_{e=1}^{N_e} s_e \sum_{j \in l(e)} \delta_b(\mathbf{x} - \mathbf{x}_j) \left[\frac{1}{c} p(\mathbf{x}_j, t) \right], \quad \mathbf{x}_j \in \partial\nu. \end{aligned} \quad (46)$$

It must be emphasized here that the assumption $\mathbf{n}' \cdot [\mathbf{x}_\delta / x_\delta] = 1$ may not be true.

5.2.4. \mathcal{S}_f in terms of a $d-1$ -dimensional dipole source p . This subsection explains how the system of coupled first-order wave equations (41) solves the time-domain dipole integral formula (34), which is defined in terms of a dipole source p confined to a surface. Accordingly, a vector-valued force source \mathcal{S}_f is defined as:

$$\begin{aligned} \mathcal{S}_f(\mathbf{x}, t) &= a_p \int_{\partial\nu} dS'(\mathbf{x}') \delta(\mathbf{x} - \mathbf{x}') \left[\frac{1}{\rho_0} p(\mathbf{x}', t) \mathbf{n}'(\mathbf{x}') \right] \\ &\approx \frac{a_p}{N_{l(e)}} \sum_{e=1}^{N_e} s_e \sum_{j \in l(e)} \delta_b(\mathbf{x} - \mathbf{x}_j) \left[\frac{1}{\rho_0} p(\mathbf{x}_j, t) \mathbf{n}(\mathbf{x}_j) \right], \quad \mathbf{x}_j \in \partial\nu, \end{aligned} \quad (47)$$

where \mathbf{n}' is the unit vector normal to the surface of the source.

For each individual node j , solving the system (41) with a force source defined by Eq. (47) is equivalent to solving the wave equation:

$$\left[\frac{1}{c^2} \frac{\partial^2}{\partial t^2} - \nabla^2 \right] \tilde{p}(\mathbf{x}, t) \approx \nabla \delta_b(\mathbf{x} - \mathbf{x}_j) \cdot [-p(\mathbf{x}_j, t) \mathbf{n}(\mathbf{x}_j)], \quad (48)$$

where \tilde{p} has nonphysical units of Pa m⁻².

The semi-numerical system (41), which employs $\mathcal{S}_m = 0$ and a force source \mathcal{S}_f defined by Eq. (47), is significant from the perspective of inverse problems. By assuming p represents the pressure data measured in time on a surface, the force source (47), expressed in terms of time-reversed p , can be used to describe the *back-projected* wavefields.

In iterative frameworks such as error minimization algorithms [26, 27, 29] or *Neumann series* iterations [23, 28], the force source is defined in terms of a time-reversed variant of the residual, which represents the discrepancy between the measured and approximated wavefields on a boundary surface.

5.3. **Full-discretisation on a regular grid.** This section explains the procedure for discretising the wave equation system (41), with an emphasis on the inclusion of sources in the wave equation. Note that for approximating the time-domain primary formula (12), the generalized mass source \mathcal{S}_m should be replaced by s_m . For approximating the time-domain *monopole* formula (32), the generalized mass source \mathcal{S}_m is defined in terms of a monopole source $-\partial p / \partial \mathbf{n}$ or its equivalent $\rho_0 \partial u^n / \partial t$. Additionally, for approximating the time-domain *dipole* integral formula (34), a vector-valued force source \mathcal{S}_f is defined in terms of pressure p , confined to a surface, which acts as a dipole source.

5.3.1. *Discretized algorithm.* Let $\mathbf{X} = \{\mathbf{X}^\zeta : \zeta \in \{1, \dots, d\}\}$ with ζ representing the Cartesian coordinates and Δx^ζ the grid spacing along the Cartesian coordinate ζ . Furthermore, $\mathbf{t} \in \{1, \dots, N_t\}$ represents the time steps sampled within the measurement period $t \in \{0, \dots, T\}$, with N_s denoting the sampled time associated with the turn-off time of source radiation, T_s . A bar notation is used to specify quantities in the fully-discretized domain. The discretization of the wave equation system (41) on a grid staggered in space and time is outlined in Algorithm 1.

In Algorithm 1, $\Lambda^\zeta = e^{-\alpha^\zeta \Delta t / 2}$ is a direction-dependent Perfectly Matched Layer (PML), with α^ζ being the virtual absorption coefficient of the PML along the Cartesian coordinate ζ . Additionally, $\bar{\mathcal{S}}_m^\zeta = (1/d) \bar{\mathcal{S}}_m$, where $\bar{\mathcal{S}}_m$ is computed via a discretisation of formulas (44) and (46). Note that, as opposed to the velocity vector $\bar{\mathbf{u}}$, the acoustic density $\bar{\rho}$ is a scalar; however, it has been virtually assumed to be vector-valued to align with the direction-dependent PML.

Algorithm 1 Full-discretization at time step $\mathbf{t} \in \{1, \dots, N_t - 1\}$

- 1: **Input:** $\bar{c}; \bar{\rho}_0; \Delta t; \Lambda^\zeta$ ($\zeta \in \{1, \dots, d\}$); $\bar{\mathcal{S}}_m(\mathbf{X}, \mathbf{t} + \frac{1}{2})$; $\bar{\mathcal{S}}_f(\mathbf{X}, \mathbf{t})$
 - 2: **Initialise:** $p(\mathbf{X}, 1) = 0$; $\bar{\rho}(\mathbf{X}, 1) = 0$; $\bar{\mathbf{u}}(\mathbf{X}, \frac{1}{2}) = 0, \forall \mathbf{X}$ ▷ Set Cauchy conditions
 - 3: **Start at iteration** $\mathbf{t} = 1$
 - 4: **Record** $\bar{p}(\mathbf{X}, \mathbf{t})$
 - 5: $\bar{\mathbf{u}}^\zeta(\mathbf{X}, \mathbf{t} + \frac{1}{2}) \leftarrow \Lambda^\zeta \left[\Lambda^\zeta \bar{\mathbf{u}}^\zeta(\mathbf{X}, \mathbf{t} - \frac{1}{2}) - \Delta t \frac{1}{\bar{\rho}_0(\mathbf{X})} \frac{\partial}{\partial \zeta} \bar{p}(\mathbf{X}, \mathbf{t}) \right] + \Delta t \bar{\mathcal{S}}_f^\zeta(\mathbf{X}, \mathbf{t})$ ▷ Update \mathbf{u}
 - 6: $\bar{\rho}(\mathbf{X}, \mathbf{t} + 1) \leftarrow \Lambda^\zeta \left[\Lambda^\zeta \bar{\rho}(\mathbf{X}, \mathbf{t}) - \Delta t \bar{\rho}_0(\mathbf{X}) \frac{\partial}{\partial \zeta} \bar{\mathbf{u}}^\zeta(\mathbf{X}, \mathbf{t} + \frac{1}{2}) \right] + \Delta t \bar{\mathcal{S}}_m^\zeta(\mathbf{X}, \mathbf{t} + \frac{1}{2})$ ▷ Update ρ
 - 7: $\bar{p}(\mathbf{X}, \mathbf{t} + 1) \leftarrow \bar{c}(\mathbf{X})^2 \sum_{\zeta=1}^d \bar{\rho}^\zeta(\mathbf{X}, \mathbf{t} + 1)$ ▷ Update p
 - 8: **Terminate at iteration** $\mathbf{t} = N_t - 1$
 - 9: **Record** $\bar{p}(\mathbf{X}, N_t)$ ▷ Record pressure at $t = T$
 - 10: **Output:** $\bar{p}(\mathbf{X}, \mathbf{t})$ ($\mathbf{t} \in \{1, \dots, N_t\}$) ▷ Recorded pressure at $t \in [0, T]$
-

Similarly, $\bar{\mathcal{S}}_f^\zeta$ is the discretised variant of the vector-valued force source (Eq. (47)) in the Cartesian coordinate ζ . Note that, as discussed above, the assumptions made in Eq. (46) are not valid; however, it will be used as a benchmark for comparison with our proposed Eq. (47).

5.3.2. *Band-limited Dirac delta function δ_b .* A Dirac delta function in the spatial domain is equivalent to 1 for all frequencies in the spatial-frequency domain. However, full-field approximation of the acoustic wave equation is done on sampled positions, which support a finite range of frequencies. Accordingly, a Dirac delta function, δ , can be replaced by a band-limited Dirac delta function, δ_b , whose approximation on a d -dimensional discretised grid and using a *Fourier* method gives

$$\delta_b(\mathbf{X} - \mathbf{x}) \approx \prod_{\zeta=1}^d \frac{1}{\Delta x^\zeta} \frac{\sin\left(\frac{\pi(X^\zeta - x^\zeta)}{\Delta x^\zeta}\right)}{N_n^\zeta \sin\left(\frac{\pi(X^\zeta - x^\zeta)}{N_n^\zeta \Delta x^\zeta}\right)}, \quad (49)$$

where $\prod_{\zeta=1}^d$ denotes the product of terms associated with the Cartesian coordinates [68]. Approximating the δ_b function using the formula (49) is computationally expensive. For sufficiently large N^ζ , the band-limited Dirac delta function can be approximated more efficiently through the formula

$$\delta_b(\mathbf{X} - \mathbf{x}) \approx \prod_{\zeta=1}^d \frac{1}{\Delta x^\zeta} \text{sinc}\left(\frac{\pi(X^\zeta - x^\zeta)}{\Delta x^\zeta}\right), \quad (50)$$

and then neglecting the magnitudes smaller than a threshold [68].

5.3.3. *Discretized mass source.* Now, plugging the band-limited Dirac delta function (50) into the formula (42) gives a full-discretized mass source

$$\bar{s}_m(\mathbf{X}, \mathbf{t}) \approx \frac{\Delta t}{N_{l(e)}} \sum_{e=1}^{N_e} v_e \sum_{j \in l(e)} \delta_b(\mathbf{X} - \mathbf{x}_j) \sum_{\mathbf{t}'=1}^{\mathbf{t}} s(\mathbf{x}_j, \mathbf{t}'). \quad (51)$$

In the same way, a full-discretization of the formulas (44) and (46), respectively, give

$$\bar{\mathcal{S}}_{(m, u^n)}(\mathbf{X}, \mathbf{t}) \approx \frac{a_p}{N_{l(e)}} \sum_{e=1}^{N_e} s_e \sum_{j \in l(e)} \delta_b(\mathbf{X} - \mathbf{x}_j) [\rho_0 u^n(\mathbf{x}_j, \mathbf{t})], \quad (52)$$

and

$$\bar{\mathcal{S}}_{(m,p)}(\mathbf{X}, \mathbf{t}) \approx \frac{a_p}{N_{l(e)}} \sum_{e=1}^{N_e} s_e \sum_{j \in l(e)} \delta_b(\mathbf{X} - \mathbf{x}_j) \left[\frac{1}{c} p(\mathbf{x}_j, \mathbf{t}) \right]. \quad (53)$$

In addition, a full-discretization of the formula (47) gives the discretized force source

$$\bar{\mathcal{S}}_f(\mathbf{X}, \mathbf{t}) \approx \frac{a_p}{N_{l(e)}} \sum_{e=1}^{N_e} s_e \sum_{j \in l(e)} \delta_b(\mathbf{X} - \mathbf{x}_j) \left[\frac{1}{\rho_0} p(\mathbf{x}_j, \mathbf{t}) \mathbf{n}'(\mathbf{x}_j) \right]. \quad (54)$$

Note that by using Eq. (53) to model a dipole surface source in terms of pressure, the assumptions $kx_\delta \gg 1$ (far-field) and $\mathbf{n}' \cdot \mathbf{x}_\delta / x_\delta$ (source omnidirectionality) are enforced. (These assumptions may not be true.) However, Algorithm 1 with $\bar{\mathcal{S}}_m = 0$ and a discretized force source $\bar{\mathcal{S}}_f$ defined by Eq. (54) directly models the original dipole integral formula (34) without any limiting assumptions. It must be reminded that in these formulas, $a_p = 2$ is set for infinite-plane apertures, and $a_p = 1$ is used for arbitrary-shaped apertures, for example cylindrical or spherical apertures.

5.3.4. Discretization of the directional gradients. In Algorithm 1, a k-space pseudo-spectral approach is used for discretization of directional gradients of fields [2, 3]. Note that the explained numerical approaches for including source in Algorithm 1, and the numerical results which will be presented in the next section, are independent of the approach taken for discretizing the directional gradients of fields.

6. NUMERICAL RESULTS

This section evaluates the accuracy of the full-field approximation of the wave equation implemented using Algorithm 1. The analysis focuses on comparing the approximated wavefields with analytic solutions for three key cases: (1) modeling the action of the primary Green's formula (12) using a mass source as defined by Eq. (51), (2) approximating the monopole integral formula (32) via a mass source defined by Eq. (52), and (3) modeling the dipole integral formula (34) using a force source as defined by Eq. (54). Initially, comparisons are made for a volumetric radiation source localized at a single point. This is then extended to simulate wavefields generated by finite-size apertures, including a monopole source distributed over a disc-shaped surface and a dipole source applied to a similar region.

Full-field approach. Wave simulations were performed using Algorithm 1. The *k-Wave* toolbox [3], which employs a k-space pseudospectral method for computing directional gradients of fields [1, 2], was used to implement this algorithm. A computational grid with sampled positions in the range $[-7.14, +7.14] \times [-7.14, +7.14] \times [-7.14, 0.5] \text{cm}^3$ and with a spacing of 0.4 mm along all Cartesian coordinates was used. The sound speed and ambient density were set to 1540ms^{-1} and 1000kgm^{-3} , respectively, in a homogeneous medium.

The maximum frequency supported by the grid for wave simulation was determined by the *Shannon-Nyquist* limit [2]. For a homogeneous medium with sound speed c , the maximum supported frequency is given by [5]:

$$f_{\max} = \frac{c}{2 \max(\Delta x^\zeta)}, \quad \zeta \in \{1, \dots, d\}, \quad (55)$$

which equals 1.925 MHz in this experiment. The time step was set to $0.04 \mu\text{s}$.

This section evaluates the full-field approach for approximating the action of a causal Green's function on a point source, as well as the *monopole* and *dipole* integral formulas derived in (32)

and (34), respectively. First, Eq. (51) is used to define the mass source in terms of a volumetric radiation source, s , located at a single point. Then, Eq. (52) is used to extend the mass source to model a monopole source confined to a disc-shaped surface with a radius of 8 mm. Finally, Eq. (54) is used to model a vector-valued force source in terms of a dipole source, p , also confined to a disc-shaped surface with a radius of 8 mm.

Analytical Approach. The accuracy of the full-field approach was evaluated by comparing its approximated wavefields with analytical solutions, which served as benchmarks. Specifically, the action of the causal Green’s function on a point source was computed analytically in the frequency domain using the primary Green’s formula (23), where the 3D Green’s function (19) acts on a point source. For a source located at a single point, the spatial integral in Eq. (23) is omitted.

Furthermore, the open-source *Field II* toolbox was employed to calculate the *monopole* integral formula (32) and the *dipole* integral formula (35) in the time domain [69, 70]². These analytical solutions were used as benchmarks to assess the performance of the full-field approximations.

In these formulations, the coefficient a_p is set to 2 for infinite-plane apertures and to 1 for apertures with arbitrary shapes, such as cylindrical or spherical surfaces.

6.1. Radiation Source, s , at a Single Point. When the volumetric radiation source, s , is defined at a single point, the spatial integral in the primary Green’s formula (12) and its equivalent frequency-domain formula (23) is eliminated. These formulas then describe the action of the causal Green’s function on a source localized at an arbitrary single point. This section evaluates the accuracy of the full-field approximation in reproducing this analytical action.

³

For a radiation source localized at an arbitrary single point \mathbf{x}_0 , Eq. (51), which defines the mass source on sampled points in space and time, simplifies to the following formula:

$$\bar{s}_m^{\text{point}}(\mathbf{X}, \mathbf{t}) \approx \Delta t \delta_b(\mathbf{X} - \mathbf{x}_0) \sum_{t'=1}^{\mathbf{t}} \bar{s}(\mathbf{x}_0, t'). \quad (56)$$

6.1.1. Experiment. A set of 40 transducers, modeled as single points, were arranged on a hemisphere centered at the origin of the Cartesian coordinate system with a radius of 5.6 cm. One transducer, located at $\mathbf{x}_0 = [0, -5.6]$ cm, was used as an emitter, excited by an ultrasonic pulse, while the remaining transducers served as receivers. Figure 1(a) illustrates the emitter and receiver positions, marked in yellow and red, respectively. The source pulse in the time domain is shown in Figure 1(b) and is quantified in terms of s .

For the point source investigated in this section, a more detailed analysis was performed by comparing results in the frequency domain. Algorithm 1 was employed to perform a time-domain full-field approximation of the action of the causal Green’s function on the source pulse. The time-domain source pulse is depicted in Figure 1(b), while its spatial distribution is represented in Figure 1(a). The approximated, nonphysical wavefield was recorded in time at all receiver positions and subsequently transformed into the frequency domain using the left equation in (16). This

²Several open-source solvers are available for analytical integral formulas used in acoustics [71, 72].

³As discussed at the beginning of Section 2, the solution of the wave equation (1) assumes the source is square-integrable in space and time. However, this condition is not satisfied for a source defined at a single point. As a result, for a point source, all quantities included in the semi-numerical system 39 are not physical quantities. Specifically, for this simplified and nonphysical numerical experiment using a d -dimensional radiation source s at a single point, these quantities will have units of m^{-d} multiplied by the units of physical quantities associated with a finite-sized source. However, integrating over a set of sampled points distributed across a finite volume of the source yields a wavefield with physically meaningful units.

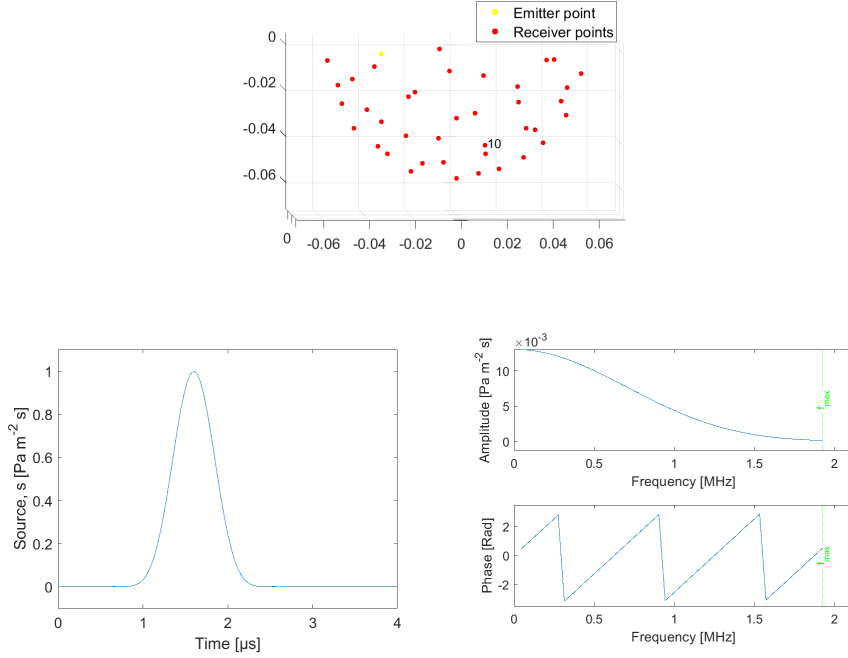


FIGURE 1. (a) A single emitter point and 39 receiver points arranged on a hemisphere with a radius of 5.6 cm, (b) the source pulse, s , represented in the time domain, (c) the source pulse, s , shown in the frequency domain, decomposed into amplitude and phase components.

transformation was performed for 50 equidistant discretized frequencies within the range $[1/50, 1] \times f_{\max}$.

For the analytical approach, the source pulse shown in Figure 1(b) was transformed into the frequency domain. Its frequency-domain representation, decomposed into amplitude and phase, is shown in Figure 1(c). The action of the frequency-domain Green's function (19) on the frequency-domain source pulse was then calculated at the selected discretized frequencies. In Figure 1(c), the green vertical line indicates f_{\max} , the maximum frequency supported by the computational grid for the full-field approximation.

6.1.2. Results. Figure 2(a) presents the amplitudes recorded at all selected sampled frequencies on Receiver 10 (as shown in Figure 1(a)). The amplitudes calculated analytically using the outgoing Green's function (19) are displayed in black, while those approximated using the full-field approach are shown in red. Similarly, Figure 2(b) illustrates the phases computed analytically and approximated via the full-field approach at all sampled frequencies on Receiver 10. These figures demonstrate a strong agreement between the analytical solution and the full-field approximation for representing the action of the causal Green's function on a point source.

Furthermore, Figures 2(c) and 2(d) depict the amplitudes and phases, respectively, approximated at a single frequency of 1 MHz across all receiver positions. These results also confirm the consistency between the analytical formula and the full-field approach for approximating the wavefield produced by the radiation source s defined at a single point.

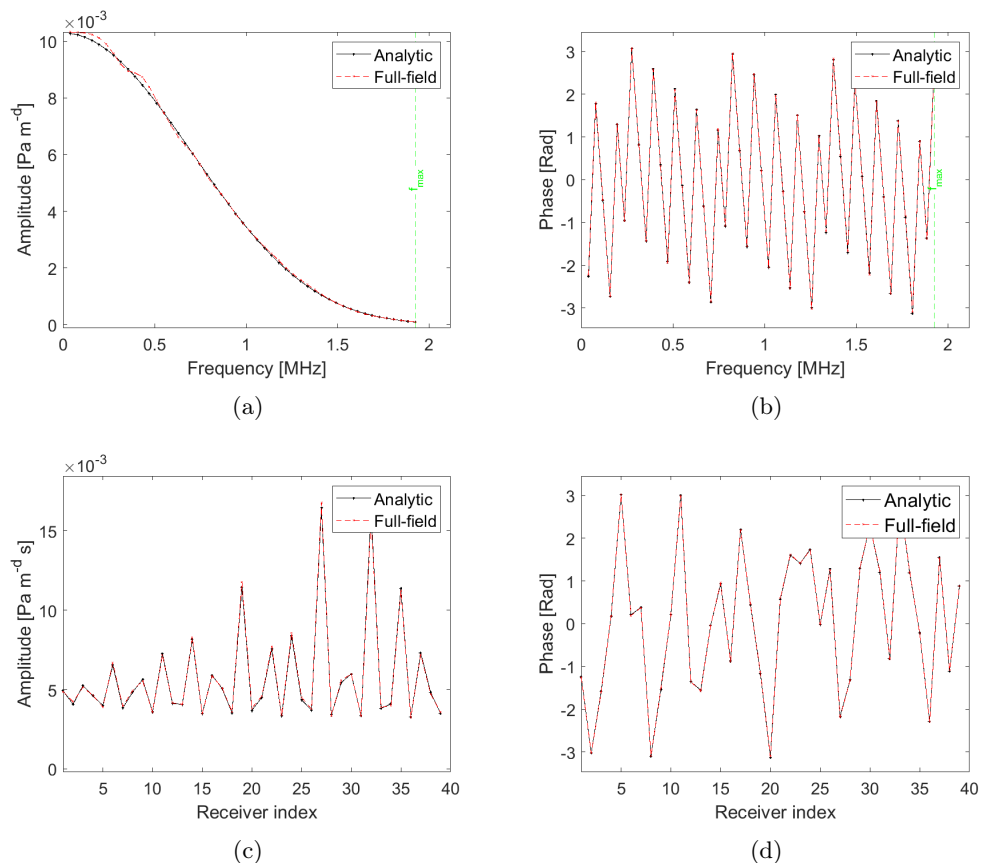


FIGURE 2. (a) Amplitude and (b) phase of the analytic action of the causal Green’s function on a source defined at a single point, evaluated at receiver 10 across all chosen frequencies. (c) Amplitude and (d) phase of the analytic action approximated at a single frequency of 1 MHz, evaluated across all receiver points.

6.2. Monopole Source Defined by Normal Velocity, u^n , on a Disc Surface. In this section, the monopole formula (32), computed analytically using the open-source *Field II* toolbox [69, 70], serves as a benchmark for assessing the accuracy of its full-field approximation derived using Algorithm 1. The mass source in the full-field approach is discretized according to Eq. (52).

6.2.1. Experiment. As explained in Section 4, the monopole integral formula (32) is derived under a rigid-baffle assumption and represents the integral of the causal Green’s function acting on a monopole source, $\rho_0 \partial u^n / \partial t$, over a surface. In this context, u^n refers to the normal component of the velocity vector relative to the source surface. The emitter, modeled as a disc-shaped surface with a radius of 8 mm and centered at the origin of Cartesian coordinates, is shown in yellow in Figure 3(a). The time-domain source pulse in terms of u^n is illustrated in Figure 3(b).

On-Grid Sampling. For the full-field approach, the wavefield must be approximated at positions sampled on a regular computational grid. The grid used for this experiment was described earlier in this section. Since the *Field II* toolbox employs an inherently analytical method, it can directly compute the wavefield at arbitrary positions. For benchmarking purposes, the analytically computed wavefield was sampled and recorded at the same positions used for the full-field approximation.

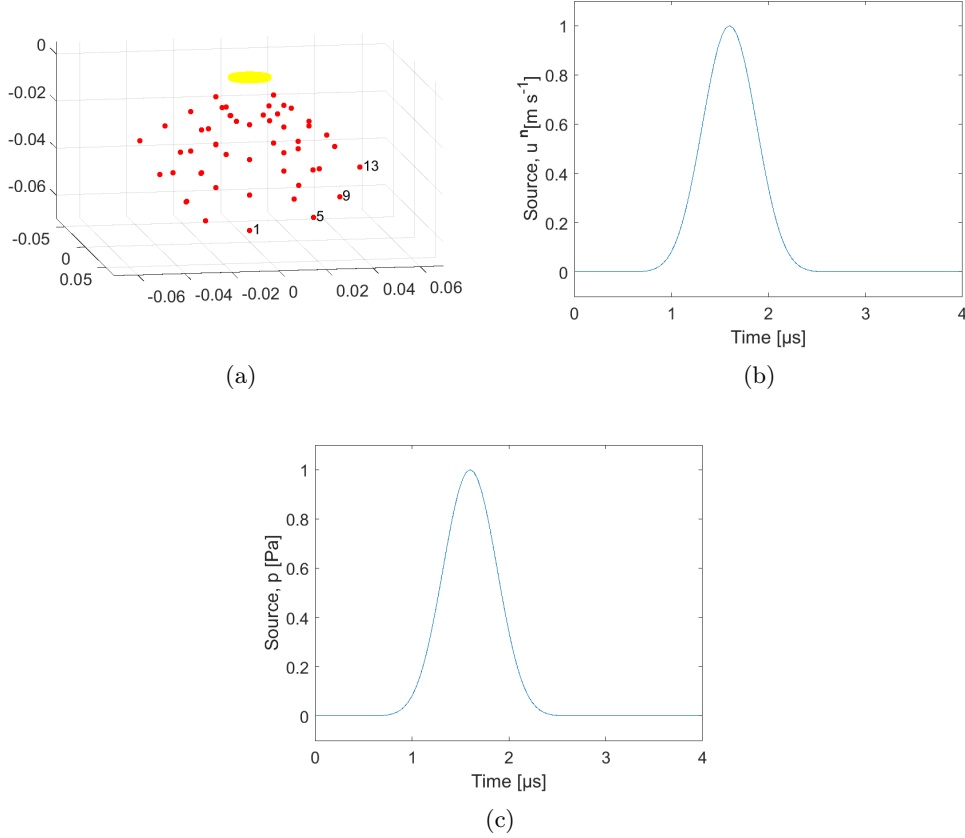


FIGURE 3. (a) A disc-shaped emitter and 64 receiver points, ordered by varying θ , φ , and r . (b) Source pulse u^n under rigid-baffle conditions. (c) Source pulse p under soft-baffle conditions.

Off-Grid Sampling. A set of 64 receiver points, positioned off the computational grid, were employed to approximate and record the wavefield. Receiver positions were defined using spherical coordinates, (r, θ, φ) . Here, distances r from the disc center (origin) were set to $\{6.5, 5, 3.5, 2\}$ cm. The polar angles φ were chosen as $\{0, \pi/6, \pi/4, \pi/3\}$, and the azimuthal angles θ were set to $\{\pi/4, 3\pi/4, 5\pi/4, 7\pi/4\}$. Receiver positions were ordered sequentially by varying θ , φ , and r .

For example, receiver positions 1–4 correspond to $r = 6.5$ cm and $\varphi = 0$, with positions differentiated by the azimuthal angle θ . Similarly, for positions 5–8, 9–12, and 13–16, $r = 6.5$ cm was maintained, but φ was incremented to $\pi/6$, $\pi/4$, and $\pi/3$, respectively. This pattern was repeated for subsequent sets of receivers, with r adjusted to 5, 3.5, and 2 cm for sets 17–32, 33–48, and 49–64, respectively.

For fixed values of r and φ , receiver positions varying by θ (e.g., sets of four consecutive receivers) are symmetric with respect to the emitter disc area. Consequently, the wavefields approximated for each set are expected to be identical. Notably, for r fixed and $\varphi = 0$, positions varying by θ overlap, resulting in 12 redundant receiver indices. These redundant indices were intentionally retained to avoid confusion in the plots. The 64 receiver positions, including the redundant ones, are shown in red in Figure 3(a) in Cartesian coordinates.

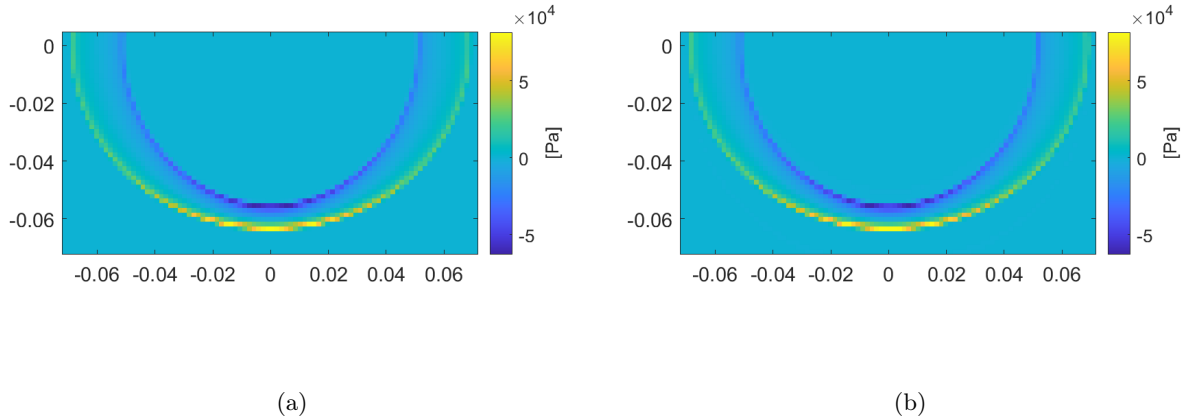


FIGURE 4. Wavefields approximated on the plane $\mathbf{x}^1 = 2.94$ cm at a single time $t = 45\mu\text{s}$, following the excitation of the disc-shaped emitter by the source pulse u^n (shown in Figure 3(b)). The emitter disc’s center is positioned at the origin of the Cartesian coordinates, as indicated in yellow in Figure 3(a) (not shown here). (a) Analytic solution using *Field II*, (b) Full-field approximation using Algorithm 1 and a mass source defined by Eq. (52).

6.2.2. *Results.* Figures 4(a) and 4(b) present the wavefields calculated analytically using the *Field II* toolbox and approximated using the full-field approach, respectively. The wavefields are shown on the grid points positioned in the plane $\mathbf{x}^1 = 2.94$ cm and at a single time instant, $t = 45 \mu\text{s}$. In both figures, the grid points are sampled with a factor of 4. Note that for both the analytic and full-field approaches, the time series approximation and recording began at $t = 0$.

These figures demonstrate a good agreement between the wavefields calculated analytically using the *Field II* toolbox and those approximated using the full-field approach.

Figures 5(a), 5(b), 5(c), and 5(d) illustrate the wavefields approximated in time at the receiver points 1, 5, 9, and 13, respectively. These receiver points are depicted in Figure 3(a). For these receiver positions, the radius and azimuthal angle are fixed at $r = 6.5$ cm and $\theta = \pi/4$, respectively. The positions are then adjusted by varying the polar angle φ . As shown in these figures, for all receiver locations, the full-field approach—using Algorithm 1 and a discretized mass source defined by Eq. 52—produces wavefield approximations that align with the corresponding analytical results calculated using the *Field II* toolbox.

Figure 6 illustrates the relative error (RE) for all 64 receiver points. The receiver positions are ordered by varying θ , φ , and r . For each set of four consecutive receiver indices (1 – 4, 5 – 8, ..., 61 – 64), φ and r remain fixed, while θ varies. Since the receiver positions adjusted only by θ are symmetric with respect to the emitter disc’s area, the computed RE values are closely aligned. Specifically, each set of receiver positions (1 – 4, 17 – 20, 33 – 36, 49 – 52), where $\varphi = 0$, are identical (redundant) and yield the same RE.

This plot demonstrates strong agreement between the full-field approach and the analytical solutions obtained using the *Field II* toolbox, underscoring the accuracy of wavefield approximations produced by the monopole surface source defined in Eq. 52 in this experiment.

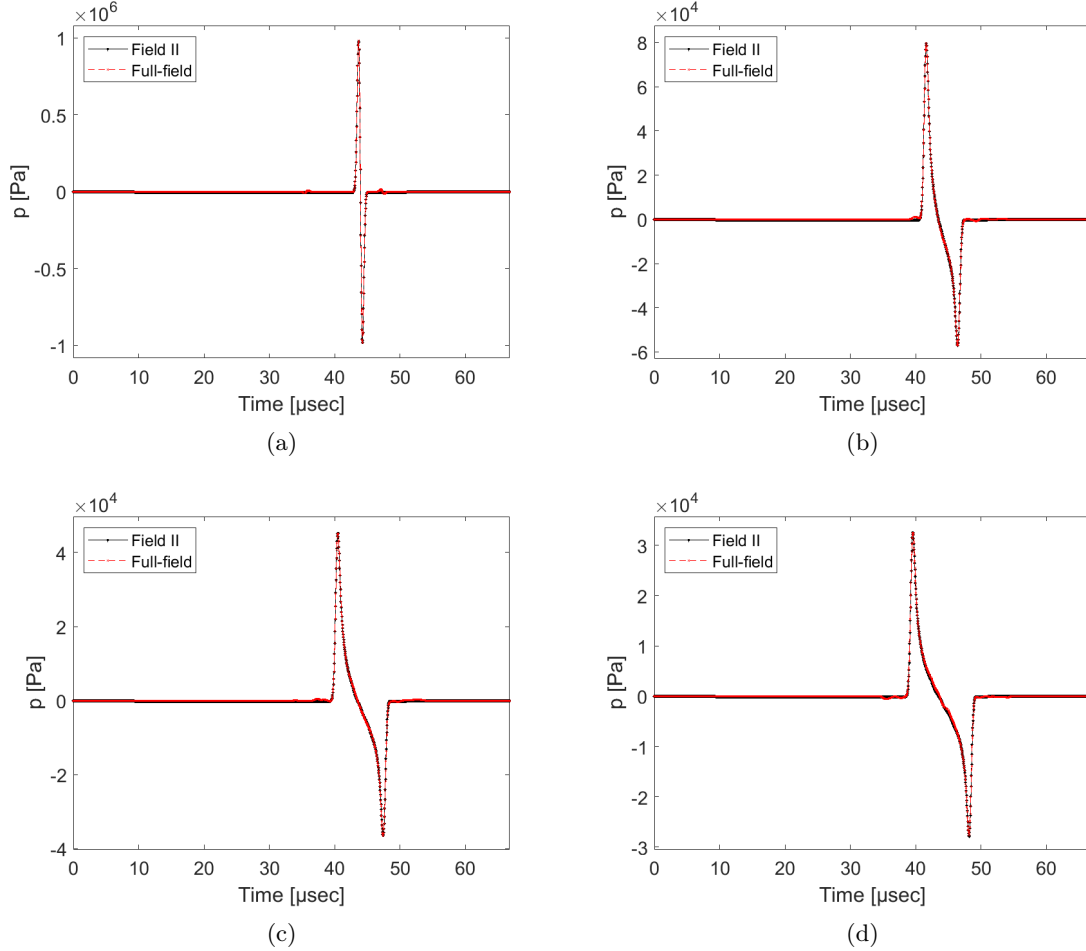


FIGURE 5. Wavefields approximated and recorded in time at receiver points following the excitation of the disc-shaped emitter by the source pulse u^n (shown in Figure 3(b)). Receiver points: (a) 1, (b) 5, (c) 9, (d) 13. The monopole integral formula (32) was approximated using both the full-field approach and the *Field II* toolbox.

6.3. Dipole Source Defined by Pressure, p , on a Disc Surface. This section compares the full-field approximation of the integral formula (34) with its analytic solution, derived through an equivalent formulation (35).

6.3.1. Experiment. The emitter disc, depicted in yellow in Figure 3(a), is excited by a source pulse p , illustrated in the time domain in Figure 3(c). Under a soft-baffle assumption, the dipole integral formula (34) is derived, representing the integral of the normal derivatives of the causal Green's function acting on a dipole source p confined to a surface. For benchmarking purposes, this formula is reformulated as an integral involving the obliquity-corrected causal Green's function acting on a surface source, split into far-field and near-field components, as presented in formula (35). The analytic approximation of the integral formula (35) is conducted using the *Field II* toolbox.

The full-field approximation of the integral formula (34) is implemented using Algorithm 1, with a force source discretized in accordance with Eq. (54).

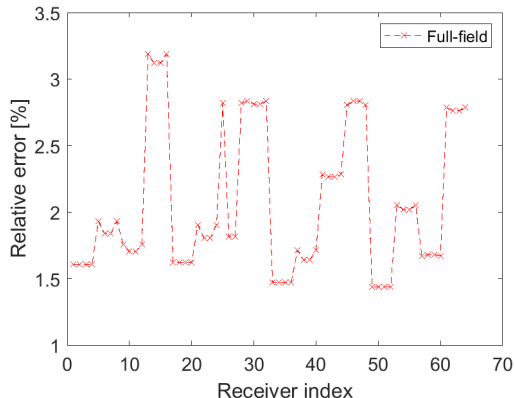


FIGURE 6. Relative error (RE) of the wavefield approximated by the full-field approach in time and at the selected receiver points following the excitation of the emitter disc by the source pulse u^n (shown in Figure 3(b)). The full-field approach utilizes Algorithm 1 and a mass source defined by Eq. (52). The wavefield analytically calculated using the *Field II* toolbox serves as the benchmark. Receiver positions are ordered by varying θ , φ , and r .

On-Grid Sampling. As discussed in Section 6.2, both the analytic and full-field approaches record the wavefield over equispaced sampling points used for the full-field approximation.

Off-Grid Sampling. Wavefields are approximated and recorded at off-grid receiver positions, displayed in red in Figure 3(a), using both analytic and full-field approaches.

6.3.2. Results. Figure 7(a) shows the wavefields calculated analytically using the dipole integral formula (35). Additionally, Figure 7(b) presents the full-field approximation of the far-field integral formula (36), computed using Algorithm 1 and a mass source defined by the discretized formula (53). As previously discussed, this approximation relies on two limiting assumptions: (1) the far-field condition $kx_\delta \gg 1$, and (2) the source is assumed omnidirectional, enforced by setting $\mathbf{n}' \cdot \mathbf{x}_\delta / x_\delta = 1$.

In contrast, Figure 7(c) illustrates the wavefield approximated using the full-field approach in Algorithm 1, with a discretized force source defined by Eq. (54). All the wavefields are evaluated at grid points in the plane $\mathbf{x}^1 = 2.94$ cm and at a single time, $t = 45$ μ s. The grid points are sampled by a factor of 4. For reference, the emitter disc's center is positioned at the origin of the Cartesian coordinates (not shown in the figure).

As seen in Figure 7(b), the limiting assumptions, particularly the omnidirectionality condition, result in discrepancies when compared to the analytic solution shown in Figure 7(a). However, as demonstrated in Figure 7(c), the full-field approximation of the dipole integral formula, implemented using a discretized force source term (Eq. (54)) and incorporated into the equation of motion in Algorithm 1, produces a wavefield that closely matches the analytically calculated wavefield.

Figures 8(a), 8(b), 8(c), and 8(d) show the wavefields approximated and recorded at receiver positions 1, 5, 9, and 13, respectively. These receiver positions are depicted in Figure 3(a). As described in Section 6.2, the receiver positions are represented in spherical coordinates for this experiment. Specifically, for the selected receiver positions, the radius r and the azimuthal angle θ are fixed at $r = 6.5$ cm and $\theta = \pi/4$, respectively. The positions vary only by the polar angle φ , resulting in changes to $\mathbf{n}' \cdot \mathbf{x}/x$ by $\cos(\varphi)$.

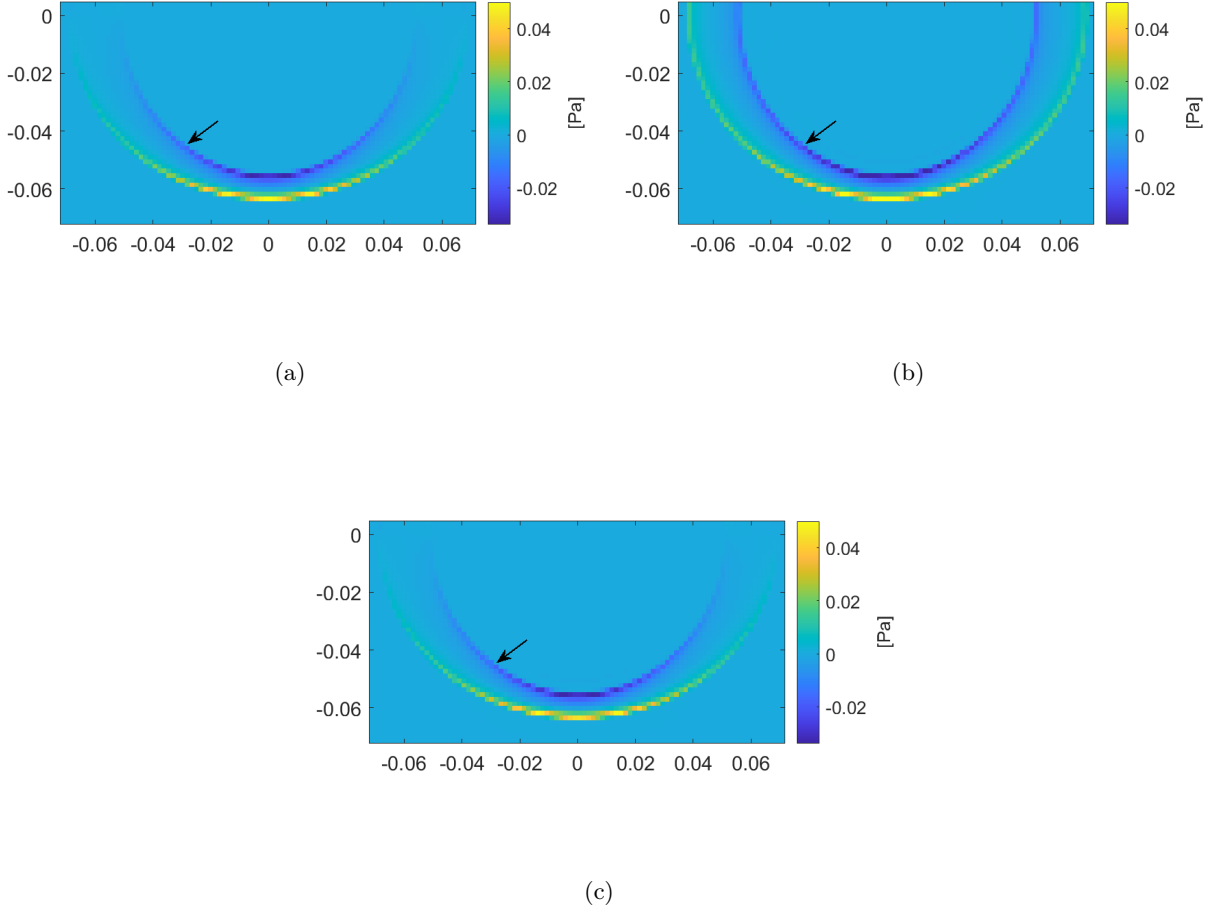


FIGURE 7. The wavefield approximated on the plane $\boldsymbol{x}^1 = 2.94$ cm and at a time of $45 \mu\text{s}$ after excitation of the disc-shaped emitter by a source pulse p , which is shown in Figure 3(c). The center of the emitter disc is placed at the origin of the Cartesian coordinates, as shown in Figure 3(a). (Not shown here.) (a) Analytic solution using *Field II*, (b) Full-field approximation using a mass source defined by Eq. (53) added to the equation of continuity, (c) Full-field approximation using a vector-valued force source defined by Eq. (54) added to the equation of motion.

As illustrated in these figures, for all the selected receiver positions, the full-field approximation of the dipole integral formula (34), computed using Algorithm 1 with a vector-valued force source (Eq. (54)), provides wavefield solutions that closely match those derived from the analytic formula. However, the wavefields approximated using the same algorithm with a mass source (Eq. (53)) exhibit significant discrepancies compared to the analytic solution obtained using the *Field II* toolbox.

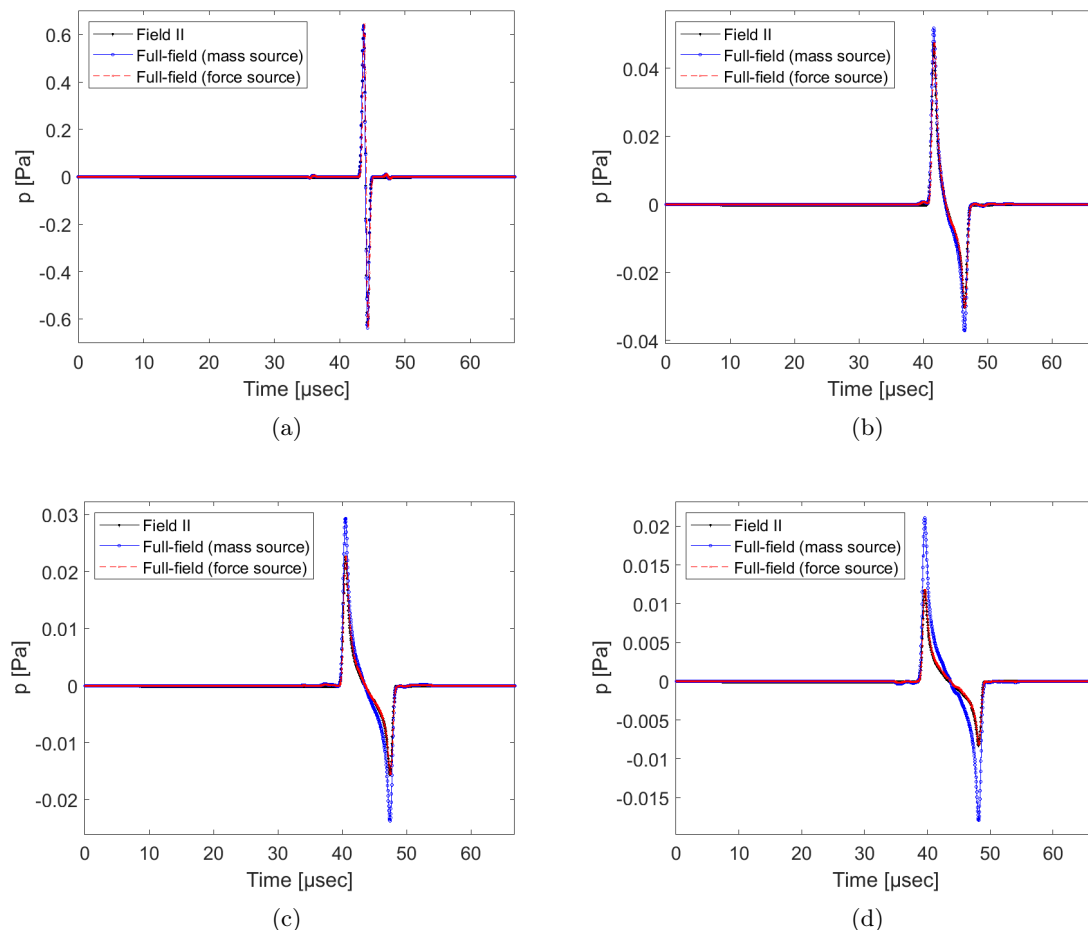


FIGURE 8. The wavefield approximated at the receivers over time after the excitation of the disc-shaped emitter by a source pulse p , as shown in Figure 3(c). Receiver points: (a) 1, (b) 5, (c) 9, (d) 13. For benchmarking, the *Field II* toolbox is used to analytically compute the dipole integral formula (35) (black). The full-field approach based on Algorithm 1 is implemented in two ways: (1) using a mass source defined by Eq. (53) added to the equation of continuity (blue), and (2) using a force source defined by Eq. (54) added to the equation of motion (red).

7. DISCUSSION AND CONCLUSION

Approaches for solving the acoustic wave equation can be broadly categorized into analytic and full-field methods. Analytic methods are suitable for homogeneous or weakly heterogeneous (smoothly varying) media, as they can account for refraction effects and singly scattered waves [69, 70, 73, 74]. In contrast, full-field approaches are well-suited for handling complex heterogeneities, sharp transitions, and higher-order scattering phenomena in acoustic media [3].

In some Geophysical applications, acoustic waves propagate with wavelengths significantly larger than the size of the acoustic aperture. For such cases, transducers are often approximated as single points [10]. However, this assumption is not applicable to many biomedical applications where high

frequencies are utilized [65, 66, 75]. Consequently, accurately approximating acoustic waves using full-field approaches requires accounting for the finite-size effects of acoustic apertures.

This study explored the equivalence between analytic and full-field approaches. Specifically, we demonstrated how isotropic mass sources and vector-valued force sources should be defined, discretized, and incorporated into the full-field approach (Algorithm 1) to ensure solutions align with their associated analytic formulas.

To achieve this, an equivalence was first established between the analytic primary formula (12), defined in terms of a volumetric radiation source s , and its equivalent full-field approximation. It was demonstrated that the full-field approach can be represented as an integral of the causal Green’s function acting on the radiation source over its volumetric and temporal support. This equivalence was numerically validated in Section 5.1.

The established equivalence between the analytic and full-field approaches for modeling the primary formula was then extended to the monopole integral formula (32). This formula describes acoustic waves in terms of a monopole source, $-\partial p/\partial \mathbf{n} = \rho_0 \partial u^n/\partial t$, confined to a finite-sized surface and directed outwardly normal to the surface.

In addition, the dipole integral formula (34) is equivalent to an integral of the normal derivatives of the causal Green’s function acting on a dipole source, p , confined to a surface. This integral formula can be reformulated into Eq. (35), which represents the wavefield as an integral of the obliquity-corrected Green’s function acting on a source split into far-field and near-field components.

The far-field formula (36) is a simplified version of Eq. (35), where the near-field source term, $p/[ct_\delta]$, has been neglected. It was shown that a full-field approximation of the far-field dipole formula (36), using Algorithm 1 and a discretized mass source defined by Eq. (53), implicitly enforces an omnidirectionality assumption, $\mathbf{n}' \cdot \mathbf{x}_\delta/x_\delta = 1$. This assumption does not hold for finite-size apertures, leading to significant errors in the approximated wavefield (Figure 7(b)) when compared to the analytic solution of the dipole formula (35) (Figure 7(a)).

In contrast, a full-field approximation of the dipole integral formula (34), implemented using Algorithm 1 with a discretized force source defined by Eq. (54), yielded a wavefield solution (Figure 7(c)) that closely matches the analytic solution obtained using the *Field II* toolbox [69, 70]. This agreement is further corroborated by the pressure profile approximated over time at receiver 10, as shown in Figure 8.

From the perspective of inverse problems, the observed match between the full-field approximation of the dipole integral formula (34) and its analytic solution is highly significant. This agreement validates the feasibility of approximating an interior-field variant of the dipole integral formula—the first term in Eq. (15)—using Algorithm 1 in conjunction with a force source defined by a time-reversed variant of Eq. (54).

In the interior-field dipole formula (15), p represents the pressure data measured in time on a boundary surface or the residual function when used in iterative frameworks, such as error minimization algorithms [26, 27, 29] or *Neumann series* iterations [23, 28]. The next step is to conduct a comprehensive evaluation—both theoretical and practical—of the derived full-field approximation of the time-reversal (back-projection) operator. This operator, which incorporates the analytic frequency-independent angular dependence of the receivers, will be compared to other established time-reversal approaches in the literature, with a focus on its integration within the *Neumann-series* framework and adjoint-assisted optimization methods for solving inverse problems in biomedical acoustics.

A key motivation lies in the fact that an analytic approximation of an interior-field variant of the dipole integral formula (Eq. (35)) has been widely utilized as the back-projection step in photoacoustic tomography for acoustically homogeneous media [65, 66]. Our study has now

extended this approach to heterogeneous media by analytically deriving and numerically validating its equivalent full-field approximation.

ACKNOWLEDGMENT

This study was conducted at the Department of Biomedical Engineering, School of Electrical and Computer Engineering, University College of Engineering, University of Tehran. The work presented in Section 6.1 was supported by the UK EPSRC Grant under Project Reference: EP/T014369/1, and carried out independently of the author’s official roles at the Department of Medical Physics & Biomedical Engineering, University College London.

REFERENCES

- [1] T. D. Mast, L. P. Souriau, D. -L. D. Liu, M. Tabei, A. I. Nachman and R. C. Waag, “A k-space method for large-scale models of wave propagation in tissue”, *IEEE Trans. Ultrason. Ferroelectr. Freq.*, vol. 48, no. 2, pp. 341-354, March 2001, doi: 10.1109/58.911717.
- [2] M. Tabei, T. D. Mast, and R. C. Waag, “A k-space method for coupled first-order acoustic propagation equations”, *J. Acoust. Soc. Am.* vol. 111, pp. 53–63, 2002.
- [3] B. E. Treeby and B. T. Cox, “k-Wave: MATLAB toolbox for the simulation and reconstruction of photoacoustic wave fields”, *J. Biomed. Opt.* vol. 15, no. 2, 021314, 2010.
- [4] S. Holm and S.P. Näsholm, “A causal and fractional all-frequency wave equation for lossy media”, *J. Acoust. Soc. Am.*, Vol. 130, no. 4, pp. 2195-2202, 2011.
- [5] B. Treeby and B. Cox, k-Wave user manual, “A Matlab toolbox for the time domain simulation of acoustic wave fields”, Version 1.1, 27th August 2016 (the last version).
- [6] S. Bilbao and B. Hamilton, “Directional Sources in Wave-Based Acoustic Simulation”, in *IEEE/ACM Transactions on Audio, Speech, and Language Processing*, vol. 27, no. 2, pp. 415-428, Feb. 2019.
- [7] M. J. Bencomo and W. W. Symes, “Discretization of multipole sources in a finite difference setting for wave propagation problems”, *J. Comput. Phys.*, vol. 386, pp. 296-322, 2019.
- [8] M. M. Cavalcanti, V. N. Domingos Cavalcanti, C. L. Frota and A. Vicente, “Stability for semilinear wave equation in an inhomogeneous medium with frictional localized damping and acoustic boundary conditions”, *SIAM J Control Optim*, Vol. 58, no. 4, pp. 2411–2445, 2020.
- [9] A. A. Alcântara, B. A. Carmo, H. R. Clark, R. R. Guardia and M. A. Rincon, “Nonlinear wave equation with Dirichlet and Acoustic boundary conditions: theoretical analysis and numerical simulation”, *Comp. Appl. Math.* Vol. 41, no. 141, 2022, <https://doi.org/10.1007/s40314-022-01822-5>.
- [10] A. Siahkoohi, M. Louboutin and F. J. Herrmann, “The importance of transfer learning in seismic modeling and imaging”, *Geophysics*, Vol. 84, no. 6, pp. A47-A52, 2019, <https://doi.org/10.1190/geo2019-0056.1>.
- [11] A. Javaherian, F. Lucka and B. Cox, “Refraction-corrected ray-based inversion for three-dimensional ultrasound tomography of the breast”, *Inverse Problems*, vol. 36, no. 12, 125010, 2020.
- [12] Y. Tang, B. Sun and T. Alkhalifah, “Wave-equation migration velocity analysis via the optimal-transport-based objective function”, *Geophysics*, Vol. 87, no. 3, pp. U109–U120, 2022.
- [13] T. Furuya and R. Potthast, “Inverse medium scattering problems with Kalman filter techniques”, *Inverse Problems*, Vol. 38, no. 9, 095003, 2022.
- [14] S. Bhattacharyya, M. V. de Hoop, V. Katsnelson and G. Uhlmann, “Recovery of wave speeds and density of mass across a heterogeneous smooth interface from acoustic and elastic wave reflection operators”, *GEM-International Journal on Geomathematics*, Vol. 13, no. 1, 2022.
- [15] H. Chauris and M. Farshad, “Seismic differential semblance-oriented migration velocity analysis — Status and the way forward”, *Geophysics*, Vol. 88, no. 6, pp. U81-U100, 2023.
- [16] M. Bader, R. G. Clapp, K. T. Nihei, and B. Biondi, “Moment tensor inversion of perforation shots using distributed-acoustic sensing”, *Geophysics*, Vol. 88, no. 6, pp. 1-36, 2023. <https://doi.org/10.1190/geo2021-0661.1>.
- [17] M. Papadopoulou, B. Brodic, E. Koivisto, A. Kaleshova, M. Savolainen, P. Marsden, and L. V. Socco, “High-resolution static corrections derived from surface-wave tomography: Application to mineral exploration”, *Geophysics*, Vol. 88, no. 6, B317-B328, 2023.

- [18] M. V. Eaid, S. D. Keating, K. A. Innanen, M. Macquet and D. Lawton, “Field assessment of elastic full-waveform inversion of combined accelerometer and distributed acoustic sensing data in a vertical seismic profile configuration”, *Geophysics*, vol. 88, no. 6, pp. WC163-WC180, 2023.
- [19] B. Kaltenbacher and W. Rundell, “On the simultaneous reconstruction of the nonlinearity coefficient and the sound speed in the Westervelt equation”, *Inverse Problems*, Vol. 39, no. 10, p. 105001, 2023, DOI 10.1088/1361-6420/aceef2.
- [20] W. Wang, G. A. McMechan and J. Ma, “Reweighted variational full-waveform inversions”, *Geophysics*, Vol. 88, no. 4, R-499-R512 <https://doi.org/10.1190/geo2021-0766.1>.
- [21] G. Uhlmann and Y. Zhang, “An inverse boundary value problem arising in nonlinear acoustics”, *SIAM Journal on Mathematical Analysis*, Vol. 55, no. 2, pp. 1364-1404, 2023.
- [22] B. Kaltenbacher and V. Nikolić, The vanishing relaxation time behavior of multi-term nonlocal Jordan–Moore–Gibson–Thompson equations, *Nonlinear Analysis: Real World Applications*, Vol. 76, pp. 103991, 2024, <https://doi.org/10.1016/j.nonrwa.2023.103991>.
- [23] J. Qian, P. Stefanov, G. Uhlmann and H. Zhao, “An Efficient Neumann series-based algorithm for thermoacoustic and photoacoustic tomography with variable sound speed”, *SIAM J. Imaging Sci.*, Vol.4, no.3, 2011. doi: 10.1137/100817280.
- [24] T. Tarvainen, B. T. Cox, J. Kaipio, and S.R. Arridge, “Reconstructing absorption and scattering distributions in quantitative photoacoustic tomography”, *Inverse Problems*, Vol. 28, 2012 ,p.084009.
- [25] R. Kowar and O. Scherzer, “Attenuation Models in Photoacoustics”. In: H. Ammari (eds) *Mathematical Modeling in Biomedical Imaging II. Lecture Notes in Mathematics*, Vol. 2035, 2012. Springer, Berlin, Heidelberg. <https://doi.org/10.1007/978-3-642-22990-94>.
- [26] X. L. Dean-Ben, A. Buehler, V. Ntziachristos and D. Razansky, “Accurate model-based reconstruction algorithm for three-dimensional optoacoustic tomography”, *IEEE T-MI*, Vol.31, no.10, pp.19221928, 2012.
- [27] A. Hauptmann et al., “Model-Based Learning for Accelerated, Limited-View 3-D Photoacoustic Tomography”, *IEEE T-MI*, vol. 37, no. 6, pp. 1382-1393, June 2018, doi: 10.1109/TMI.2018.2820382.
- [28] M. Haltmeier and L.V. Nguyen, “Analysis of iterative methods in photoacoustic tomography with variable sound speed”, *SIAM Journal on Imaging Sciences*, Vol.10,no.2,2017, doi: 10.1137/16M1104822.
- [29] A. Javaherian and S. Holman, “A continuous adjoint for photo-acoustic tomography of the brain”, *Inverse Problems*, vol. 34, no. 8, p. 085003, 2018.
- [30] A. Javaherian and S. Holman, “Direct quantitative photoacoustic tomography for realistic acoustic media”, *Inverse Problems*, vol.35,no.8,084004,2019.
- [31] S. Antholzer, M. Haltmeier and J. Schwab, “Deep-learning for photoacoustic tomography from sparse data”, *Inverse Problems in Science and Engineering*, Vol.27, no.7,pp.987-1005, 2019. doi: 10.1080/17415977.2018.1518444.
- [32] S. Guan, A. A. Khan, S. Sikdar and P. V. Chitnis, “Fully dense UNet for 2-D sparse photoacoustic tomography artifact removal”, *IEEE J. Biomed. Health. Inform.*, vol. 24, no. 2, pp. 568-576, Feb. 2020, doi: 10.1109/JBHI.2019.2912935.
- [33] S. Na and L. V. Wang, “Photoacoustic computed tomography for functional human brain imaging”, *Biomed. Opt. Express*, Vol. 12, pp. 4056-4083, 2021.
- [34] L. Nguyen, M. Haltmeier, R Kowar, and N. Do, “Analysis for full-field photoacoustic tomography with variable sound speed”, *SIAM J. Imaging Sci.*, Vol. 15, no. 3, 2022, 10.1137/21M1463409.
- [35] M. Suhonen, A. Pulkkinen, and T. Tarvainen, “Single-stage approach for estimating optical parameters in spectral quantitative photoacoustic tomography”, *J. Opt. Soc. Am.*, Vol. 41, no. 3, pp. 527-542, 2024.
- [36] H. Park, J. Yao and Y. Jing, “A frequency-domain model-based reconstruction method for transcranial photoacoustic imaging: A 2D numerical investigation”, *Photoacoustics*, Vol. 33, 2023, p. 100561.
- [37] A. Hauptmann and T. Tarvainen, (2024). “Model-Based Reconstructions for Quantitative Imaging in Photoacoustic Tomography”. In: Xia, W. (eds) *Biomedical Photoacoustics*. Springer, Cham. https://doi.org/10.1007/978-3-031-61411-8_4
- [38] Y. Luo et al., “Full-wave image reconstruction in transcranial photoacoustic computed tomography using a finite element method,” in *IEEE T-MI*, doi:10.1109/TMI.2024.3456595.
- [39] F. Li, U. Villa, N. Duric and M. A. Anastasio, “A forward Model incorporating elevation-focused transducer properties for 3-D full-waveform inversion in ultrasound computed tomography”, *IEEE T-UFFC*, vol. 70, no. 10, pp. 1339-1354, Oct. 2023, doi: 10.1109/TUFFC.2023.3313549.
- [40] G. Y. Sandhu, C. Li, O. Roy, S. Schmidt and N. Duric, “Frequency domain ultrasound waveform tomography: breast imaging using a ring transducer”, *Phys. Med. Biol.*, Vol. 60, 5381–5398, 2015.

- [41] A. V. Goncharsky and S. Y. Romanov, “Iterative methods for solving coefficient inverse problems of wave tomography in models with attenuation”, *Inverse Problems*, vol. 33, pp. 025003, 2017.
- [42] J. W. Wiskin, D. T. Borup, E. Iuanow, J. Klock and M. W. Lenox, “3-D Nonlinear Acoustic Inverse Scattering: Algorithm and Quantitative Results”, *IEEE T-UFFC*, vol. 64, no. 3, 2017.
- [43] L. Guasch, O. Calderón Agudo, M. Tang, P. Nachev, and M. Warner, “Full-waveform inversion imaging of the human brain”. *Nature Digital Medicine*, vol. 3, 28, 2020.
- [44] F. Faucher and O. Scherzer, “Adjoint-state method for Hybridizable Discontinuous Galerkin discretization”, application to the inverse acoustic wave problem”, *Comput. Methods Appl. Mech. Eng.*, Vol. 372, pp. 113406, 2020.
- [45] I. E. Ulrich, S. Noe, C. Boehm, N K Martiartu, B Lafci, X. L. Dean-Ben, D. Razansky and A.Fitchner, “Full-waveform inversion with resolution proxies for in-vivo ultrasound computed tomography”, 2023 IEEE International Ultrasonics Symposium (IUS), Montreal, QC, Canada, 2023, pp. 1-4, doi: 10.1109/IUS51837.2023.10308297.
- [46] D. Schweizer, R. Rau, C. D. Bezek, R. A. Kubik-Huch and O. Goksel, “Robust Imaging of Speed of Sound Using Virtual Source Transmission”, in *IEEE T-UFFC*, Vol. 70, no. 10, pp. 1308-1318, 2023.
- [47] Z. Zeng, Y. Zheng, Y. Zheng, Y. Li, Z. Shi Aand H. Sun, “Neural Born series operator for biomedical ultrasound computed Tomography”, 2023, <https://arxiv.org/abs/2312.15575>.
- [48] S. Operto, A. Gholami, H. S. Aghamiry, G. Guo, S. Beller, K. Aghazade, F. Mamfoumbi, L. Combe and A. Ribodetti, “Extending the search space of full-waveform inversion beyond the single-scattering Born approximation: A tutorial review”, *Geophysics*, Vol. 88, no. 6, pp. R671–R702, 2023. doi: <https://doi.org/10.1190/geo2022-0758.1>.
- [49] M. Soleimani, T. Rymarczyk and G. Kłosowski, “Ultrasound Brain Tomography: Comparison of Deep Learning and Deterministic Methods”, in *IEEE Trans. Instrum. Meas.*, Vol. 73, pp. 1-12, 2024, Art no. 4500812, doi: 10.1109/TIM.2023.3330229.
- [50] L. Borcea, J. Garnier, A. V. Mamonov and J. Zimmerling, “Waveform inversion with a data driven estimate of the internal wave”, *SIAM J. Imaging Sci.*, Vol. 16, no. 1, pp. 280-312, 2023, <https://doi.org/10.1137/22M1517342>.
- [51] A. Pulkkinen, B. Werner, E. Martin and K. Hynynen, “Numerical simulations of clinical focused ultrasound functional neurosurgery”, *Physics in Medicine & Biology*, vol. 59, no. 7, p. 1679, 2014.
- [52] A. Kyriakou, E. Neufeld, and B. Werner, G. Székely and N. Kuster, “Full-wave acoustic and thermal modeling of transcranial ultrasound propagation and investigation of skull-induced aberration correction techniques: a feasibility study”. *J Ther Ultrasound*, Vol. 3, no. 11, 2015. <https://doi.org/10.1186/s40349-015-0032-9>.
- [53] J. K. Mueller, L. Ai, P. Bansal and W. Legon, “Numerical evaluation of the skull for human neuromodulation with transcranial focused ultrasound”, *J. Neural Eng.*, Vol. 14, p.066012 (19pp), 2017.
- [54] S. Pichardo, C. Moreno-Hernandez, R. Andrew Drainville, V. Sin, L. Curiel, and K. Hynynen, “A viscoelastic model for the prediction of transcranial ultrasound propagation: Application for the estimation of shear acoustic properties in the human skull”, *Phys. Med. Biol.* Vol. 62, no. 17, pp. 6938–6962, 2017.
- [55] C. Pasquinelli, L.G. Hanson, H.R. Siebner, H.J. Lee and A. Thielscher, “Safety of Transcranial focused ultrasound stimulation: A systematic review of the state of knowledge from both human and animal studies”, *Brain Stimul.*, Vol. 12, no. 6, pp. 1367-1380, 2019. doi: 10.1016/j.brs.2019.07.024. Epub 2019 Jul 31. PMID: 31401074.
- [56] P. Gaur, K.M. Casey, J. Kubanek, N. Li, M. Mohammadjavadi, Y. Saenz, G.H. Glover, D.M. Bouley and K.B. Pauly. “Histologic safety of transcranial focused ultrasound neuromodulation and magnetic resonance acoustic radiation force imaging in rhesus macaques and sheep”. *Brain Stimul.* 2020 May-Jun;13(3):804-814. doi: 10.1016/j.brs.2020.02.017. Epub 2020 Feb 21. PMID: 32289711; PMCID: PMC7196031.
- [57] T. Bancel et al., “Comparison Between Ray-Tracing and Full-Wave Simulation for Transcranial Ultrasound Focusing on a Clinical System Using the Transfer Matrix Formalism”, in *IEEE T-UFFC*, vol. 68, no. 7, pp. 2554-2565, July 2021, doi: 10.1109/TUFFC.2021.3063055.
- [58] J-F Aubry, O. Bates, C. Boehm, K. B. Pauly, D. Christensen, C. Cueto, P. Gélât, L. Guasch, J. Jaros, Y. Jing, R. Jones, N. Li, P. Marty, H. Montanaro, E. Neufeld, S. Pichardo, G. Pinton, A. Pulkkinen, A. Stanzola, A. Thielscher, B Treeby and E. V. Wout, “Benchmark problems for transcranial ultrasound simulation: Inter-comparison of compressional wave models”, *J. Acoust. Soc. Am.*, vol. 152, pp. 1003–1019, 2022.
- [59] J-F Aubry, D. Attali, M. Schafer, E. Fouragnan, C. Caskey, R. Chen, G. Darmani, E. J. Bubrick, J. Sallet, C. Butler, C. Stagg, M. Klein-Flugge, S-S Yoo, B. Treeby, L. Verhagen and K. B. Pauly, “ITRUSST Consensus on Biophysical Safety for Transcranial Ultrasonic Stimulation”, 2023.
- [60] K. R. Murphy, T. Nandi, B. Kop, T. Osada, M. Lueckel, W. A. N’Djin, K. A. Caulfield, A. Fomenko, H. R Siebner, Y. Ugawa, L. Verhagen, S. Bestmann, E. Martin, K. B. Pauly, E. Fouragnan and T. O. Bergmann, “A practical guide to transcranial ultrasonic stimulation from the IFCN-endorsed ITRUSST consortium”, 2024.

- [61] S. F. Wu, “Integral formulations for predicting acoustic radiation”. *J. Acoust. Soc. Am.* 1 October 2024; 156 (4): R7–R9.
- [62] S. F. Wu, P. Zhou and Y. Lu, Determining excitation forces acting on the interior surface of an enclosure. Part I: Theory, *J. Theor. Comput. Acoust.*, Vol. 30, no. 1, 2022, 2250001.
- [63] E. V. Wout, S. R. Haqshenas, P. Gélat, T. Betcke and N. Saffari, Boundary integral formulations for acoustic modelling of high-contrast media, *COMPUT. MATH. APPL.*, Vol. 105, pp. 136-149, 2022.
- [64] R. Chen, S. Cao, W. Liu, Q. Song and Y. You, “Acoustic multipole source–simplified lattice Boltzmann method for simulating acoustic propagation problems”, *Int J Numer Meth Fluids*, vol. 95, no. 7, pp. 1174–1196, 2023.
- [65] M. Xu and L. V. Wang, “Universal back-projection algorithm for photoacoustic computed tomography”, *PHYSICAL REVIEW E*, Vol. 71, pp. 016706 (2005).
- [66] P. Burgholzer, G. J. Matt, M. Haltmeier, Markus and G. Paltauf, “Exact and approximative imaging methods for photoacoustic tomography using an arbitrary detection surface”, *Phys. Rev. E*, vol. 75, no. 4, pp. 046706, 2007, doi : 10.1103/PhysRevE.75.046706.
- [67] A.J. Devaney, “Mathematical Foundations of Imaging, Tomography and Wavefield Inversion”. Cambridge University Press; 2012.
- [68] E. S. Wise, B. T. Cox, J. Jaros and B. E. Treeby, “Representing arbitrary acoustic source and sensor distributions in Fourier collocation methods”, *J. Acoust. Soc. of Am.*, vol. 146, no. 1, pp. 278-288, 2019.
- [69] J.A. Jensen: “Field: A Program for Simulating Ultrasound Systems”, Paper presented at the 10th Nordic-Baltic Conference on Biomedical Imaging Published in *Med. Biol. Eng. Comput.*, pp. 351-353, Vol. 34, Supplement 1, Part 1, 1996.
- [70] J.A. Jensen and N. B. Svendsen: “Calculation of pressure fields from arbitrarily shaped, apodized, and excited ultrasound transducers”, *IEEE T-UFFC.*, Vol. 39, pp. 262-267, 1992.
- [71] J. F. Kelly and R. J. McGough. “A Time-Space Decomposition Method for Calculating the Nearfield Pressure Generated by a Pulsed Circular Piston”, *IEEE T-UFFC*, Vol. 153, pp. 1150-1159, 2006.
- [72] D. Garcia and F. Varray, “SIMUS3: An open-source simulator for 3-D ultrasound imaging”, *Comput. Methods. Programs. Biomed.*, Vol. 250, pp. 108169, 2024.
- [73] A. Javaherian and B. Cox, “Ray-based inversion accounting for scattering for biomedical ultrasound tomography”, *Inverse Problems*, vol. 37, no.11, 115003, 2021.
- [74] A. Javaherian, “Hessian-free ray-born inversion for high-resolution quantitative ultrasound tomography”, 2023, <https://arxiv.org/abs/2211.00316>.
- [75] J. Park, S. Choi, F. Knieling, B. Clingman, S. Bohndiek, L. V. Wang and C. Kim, “Clinical translation of photoacoustic imaging”. *Nat Rev Bioeng*, 2024.